Journal of
Materials Chemistry A

REVIEW

View Article Online
View Journal | View Issue

Cite this: *J. Mater. Chem. A*, 2019, 7, 23662

Review on anionic redox in sodium-ion batteries

Hang Xu,[a] Shaohua Guo *[a] and Haoshen Zhou[ab]

Rechargeable sodium-ion batteries (SIBs) have attracted a surge of interest as one of the most promising candidates for large-scale energy storage owing to their abundant natural resources and relatively high economic efficiency. However, the energy density provided by redox from transition metal ions has already been substantially studied and is approaching its limits. It is promising to break through the dilemma from a new aspect. Recently, the transformational anionic redox that has been widely investigated in lithium-rich layered cathodes has also been applied in SIBs; it has turned out to be an effective way to achieve worthwhile specific capacity and peculiar structural evolution. It is noteworthy that the anionic redox reaction can occur in both Na-deficient and Na-rich materials, which is different from that in lithium-ion batteries. This suggests that new electrochemistry could emerge in Na-based materials, providing opportunities to discover advanced materials and new chemistries. In this review, a systematic overlook of the published research on anionic redox in SIBs is provided, along with a discussion on the related theories that explain the mechanism of activating and stabilizing the anionic redox activity. Furthermore, current challenges and possible approaches for improvements are outlined. Further, we have summarized a variety of characterization techniques for investigating the anionic redox process. It is hoped that this review could further the understanding of the anionic redox activity in SIBs and provide an impetus to the development of advanced electrode materials for fabricating high-capacity SIBs that utilize the anionic redox reaction.

Received 14th June 2019
Accepted 9th September 2019

DOI: 10.1039/c9ta06389g

rsc.li/materials-a

1. Introduction

With the rapid development of modern society, global demand for energy consumption is booming. It is necessary to search for clean renewable energy sources to prevent environmental contamination arising from the burning of fossil fuels. As intermittent energy generation technologies have become more

Hang Xu received her bachelor's degree in material physics from Nanjing University in 2018. She is currently pursuing her Master's studies in energy materials and devices at the College of Engineering and Applied Sciences, Nanjing University. Her major research interests focus on sodium-ion batteries and related energy-storage materials.

Shaohua Guo received his PhD from the University of Tsukuba in 2015, after which he worked as a postdoctoral researcher at the National Institute of Advanced Industrial Science and Technology (AIST). He is currently an Associate Professor in the College of Engineering and Applied Sciences, Nanjing University. His research interest involves energy materials and chemistry for lithium-ion batteries, sodium-ion batteries, and solid-state batteries. He has published over 50 peer-reviewed papers in Energy & Environmental Science, Nat Commun, Angew Chem Int Ed, Adv Mater, and so on.

---

[a] *Center of Energy Storage Materials & Technology, College of Engineering and Applied Sciences, Jiangsu Key Laboratory of Artificial Functional Materials, National Laboratory of Solid State Microstructures, Collaborative Innovation Center of Advanced Microstructure, Nanjing University, Nanjing 210093, China. E-mail: shguo@nju.edu.cn*

[b] *National Institute of Advanced Industrial Science and Technology (AIST), Umezono 1-1-1, Tsukuba, 305-8568, Japan*

prevailing and integrated into the grid, it has become essential to improve the technology for large-scale energy storage.[1] Commercialized lithium-ion batteries have been widely utilized in electronic devices and power equipment, but the limited and maldistributed natural resources along with the increasing price of raw materials due to soaring market demand limit the application of lithium-ion batteries in large-scale energy storage.[2,3] Recently, sodium-ion batteries (SIBs) have been extensively studied because of earth-abundant and widespread sodium resources and the low cost facilitated by mature extraction technologies.[4–8] The practical applications of SIBs need to overcome the obstacle of the relatively small capacity of cathodes. Extensive studies have been reported to introduce outstanding electrode materials with various strategies such as doping modification, surface treatment, and composite construction.[9–12] The capacity obtained from cationic redox is close to the theoretical value and can only be increased from other strategies such as introducing anionic redox reactions.[13–15] In fact, anionic redox has been developed early in lithium-ion batteries since lithium-rich materials have been found to deliver extraordinary capacity exceeding the theoretical values.[15–19] This strategy has been recently applied to SIBs and several related articles have been published.[20–25] However, the intrinsic origin of the reaction mechanism is still under debate and it seems improper to completely transpose the theories of anionic redox from Li- to Na-based systems.[24,26,27] Therefore, it is appropriate to provide a summary of the published articles on anionic redox in SIBs and facilitate a better understanding of the fundamental principles of anionic redox reactions.

In this review, we will first simply retrospect the emergence and development of anion redox. Then, the current fundamental science and theories will be introduced, including triggering requisite, redox mechanism, as well as reversibility. Earlier studies involving anionic redox in SIBs will be systematically revisited at a later stage, catering to electronic/crystal structure, electrochemical performance, redox mechanism, and structural evolution. After analyzing the present challenges and possible approaches for reversible anionic redox in SIBs, a variety of effective characterization techniques will be discussed.

1.1 Emergence and development of anionic redox

The history of anionic redox, particularly in terms of the underlying science, can be traced back to the original sulfide electrode. Rouxel *et al.* pioneered a theory of ligand–hole chemistry in sulfides, such as TiS_3 and FeS_2.[28] In these materials, sulfur can stabilize in a more oxidized state than S^{2-} since the transition-metal (TM) d band penetrates into the ligand sp band such that some of the sp electrons get poured into the d band, leaving behind holes. Since oxides are not as covalent as sulfides, anion redox in oxides was not conceived until the successful preparation of fully delithiated Li_0CoO_2, where it was found that Co was not fully oxidized to 4^+ and the O–O interplanar distances were observed to be shortened.[29] Based on the above results, the participation of oxygen in the redox action was proposed and supported by theoretical papers predicting oxygen as the electron donor rather than TMs in $LiAl_{1-y}Co_yO_2$.[30,31] However, an unusual phenomenon remained neglected for a long time until the pivotal exploration of Li_2MnO_3 or also known as $Li[Li_{1/3}Mn_{2/3}]O_2$, wherein one-third Mn in the TM layer was replaced by Li in an ordered honeycomb-type arrangement.[15] This compound contains excess Li than usual; therefore, it was later termed as Li-rich layered oxides. Because the Mn(v)/Mn(iv) redox couple lies far below the top of the O 2p bands, it is believed that the octahedral-site Mn(v) states in oxides are not possible.[32,33] The electrochemical activity of Li_2MnO_3 can only be ascribed to the oxygen activity.[18,34] Researchers have proposed several possibilities to explain this phenomenon, including irreversible oxygen loss with surface densification,[35,36] oxygen release and reaccommodation,[37] and bulk lattice oxygen redox.[38,39] Anionic redox together with additional Li ions have remarkably increased the reversible capacity from a new perspective; this intriguing discovery has sparked the extensive attention and related research such involving Li_2RuO_3, Li_2IrO_3, and a series of extended materials by partial chemical substitutions.[15,40–42] There are several questions under intensive debate, namely, what is the pivotal requisite to activate anionic redox, details of how oxygen ions contribute toward charge compensation, and how the structure evolves during the redox process.[37–39,43] Along with the rapid development of SIBs, it is envisaged that the application of oxygen redox reactions will not be limited to LIBs and the strategy of Li substitution could be extended to other elements.[44–47] Based on this concept, a number of materials have been reported, and they have demonstrated excellent performances. This provides a new possibility for SIBs to be practically applied to large-scale energy storage applications.[20,48,49]

2. Fundamental science and mechanism of anionic redox

From the perspective of energy band theory, the energy band structure of Li-/Na-based layered TM oxides mainly involves orbital overlaps between the d orbitals of TM and p orbitals of oxygen, which is reflected in the energy spectrum as the bonding (M–O) and antibonding (M–O)* bands.[48] In general, the antibonding (M–O)* band near the Fermi level provides electrons with holes left upon charging, which is the case for the earlier single-cationic redox.[50] The capacity obtained from traditional single-cationic redox is limited because the antibonding (M–O)* band is the only source of electrons. The stabilized bonding (M–O) band is the basis for maintaining the structural integrity of materials and therefore cannot provide electrons (Fig. 1a).[51]

Some conventional layered oxides ($LiMO_2$) are found to undergo anion redox in lithium-ion batteries, represented by $LiCoO_2$. Generally, TMs on the right-hand side of the periodic table, such as Co, Ni, and Cu, have large electronegativities and have highly covalent bonds with oxygen, leading to the overlap between M(d) and L(p) states. When Li is extracted from Li_xCoO_2, the Fermi level gets pinned on top of the L(p) band and electron transfer occurs on the ligand, namely, anionic redox.

Recently, some special structures have been found to have unusual band structures, and their common feature is the introduction of the nonbonding oxygen state.[52] It is widely known that three 2p orbitals of oxygen participate in the formation of the M–O bond in classical AMO_2 (A: alkali metal; M: TM) materials.[53] However, in some special materials (*e.g.*, the early discovered lithium-rich Li_2MO_3), since one-third of the TMs are replaced by Li, one of the oxygen 2p orbitals directed toward Li is weakly bonded due to the comparatively small overlap between the O 2p orbital and Li 2s orbital.[18,54] This will induce a new energy level located above the bonding (M–O) band in the band structure, which can be utilized for providing excess electrons and delivering capacity along with circumventing structural deterioration.[51] This mechanism is termed as the Li–O–Li configuration, and the specific O 2p orbital is also sometimes called the lone-pair oxygen or the unhybridized O 2p state.[54] The average number of oxygen lone pairs is determined by the x stoichiometry of $A[A_xM_{1-x}]O_2$. When x is up to 2/3, only one TM on average is around the oxygen, leaving 2 lone pairs per oxygen.[52] In addition to Li–O–Li, there are some other configurations that can also induce the formation of nonbonding oxygen. For $Na_{2/3}[Mg_{1/3}Mn_{2/3}]O_2$ and $Na_{4/7}[\square_{1/7}Mn_{6/7}]O_2$, a portion of the TMs are replaced by alkaline-earth metals and TM vacancies, respectively, both of which limit the orbital overlaps and increase the oxygen lone pairs.[26,46,47] This can partially explain the reason why anionic redox can also be triggered in materials with no excess of A (Fig. 1b).

The above discussion reveals the importance of nonbonding oxygen, which is a prerequisite for initiating anion redox.[48,53,55] It should be pointed out that the possibility of realizing dual-

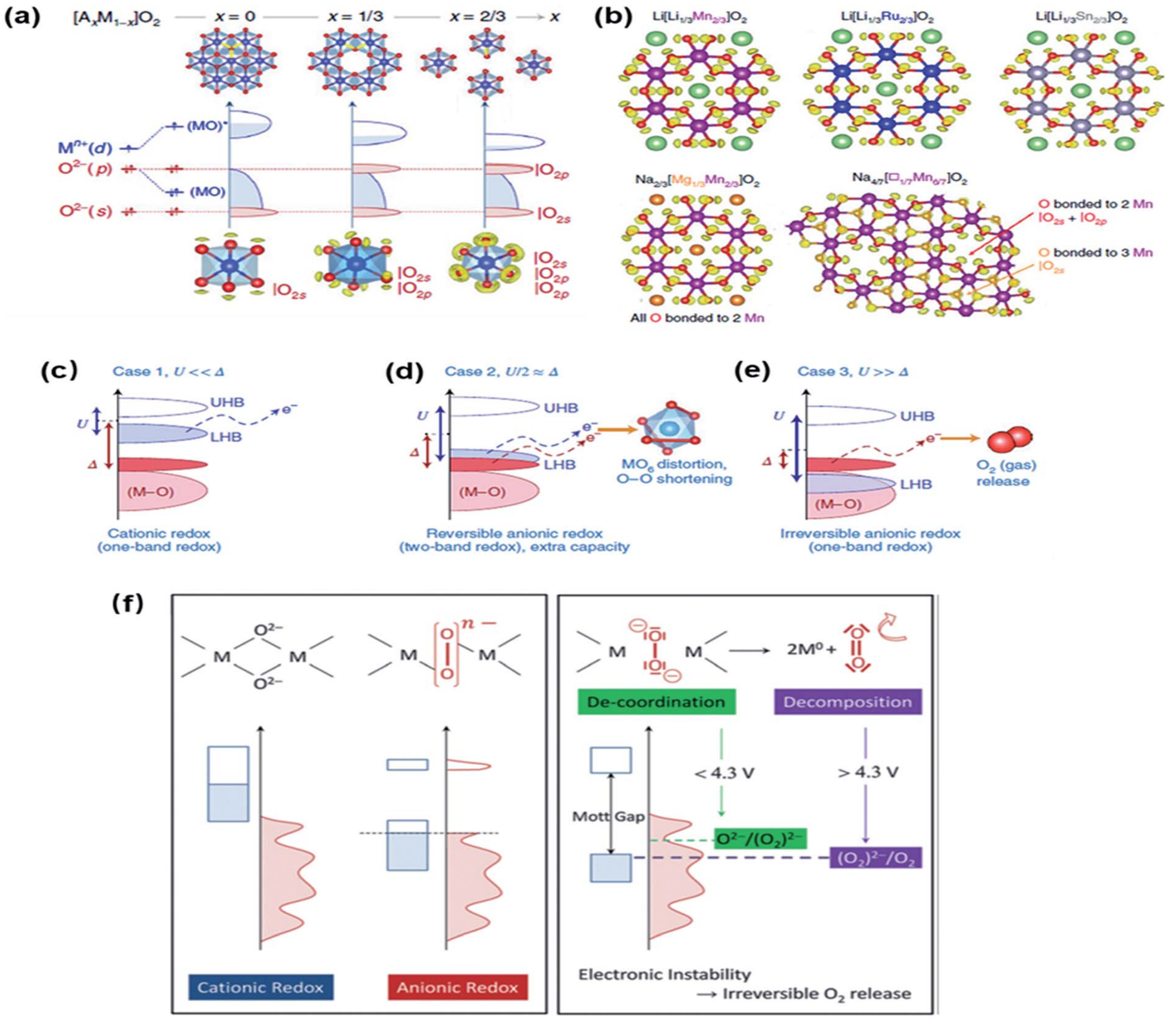

Fig. 1 (a) Schematic electronic structures of AMO_2 ($x = 0$), A_2MO_3 ($x = 1/3$), and A_5MO_6 ($x = 2/3$), where $|O_{2s}$ and $|O_{2p}$ lone-pair states are highlighted by red bands. (b) ELF computed from the first-principles DFT+U calculations (isovalues of 0.7) for $Li[Li_{1/3}M_{2/3}]O_2$ (M = Mn, Ru, Sn), showing an equivalent number of oxygen lone pairs per oxygen (one $|O_{2s}$ and one $|O_{2p}$). For $Na_{2/3}[Mg_{1/3}Mn_{2/3}]O_2$, the apparent Mn/Mg substitution can be seen as Na/Mg substitution (Mg^{2+} acting as $2Na^+$ in charge compensation); therefore, the material stoichiometry is $x = 1/3$ ("A_2MO_3"). For $Na_{4/7}[\square_{1/7}Mn_{6/7}]O_2$, one and two oxygen lone pairs per oxygen occur in the Mn-rich (orange) and Mn-poor (red) O environments, respectively. (c–e) Taking Mott–Hubbard splitting into account, the Li_2MO_3 band structure is further classified under three cases. (f) Schematic representation of the three different redox activities of a TM oxide along with the associated Lewis structures of the oxygen species.

band redox to obtain additional capacity is closely connected to the relative positions of the O 2p nonbonding and (M–O)* antibonding bands.[51] It can be qualitatively described in the Mott–Hubbard *vs.* charge transfer regimes, which are a function of U/Δ.[51] Here, Δ is the charge transfer term, which refers to the energy difference between (M–O) and (M–O)*. Its value is related to the difference in the electronegativities between M and O, reflecting the ionic–covalent nature of the M–O bond. The smaller its value, the more covalent is the bond. Here, U represents the coulombic interaction term, which represents the electron repulsive force within d orbitals, inversely proportional to the orbital volume.[56] The localized electrons cause the original (M–O)* band to split into two separate bands, namely, the upper-Hubbard band (with no electrons) and fully occupied lower-Hubbard band, termed as UHB and LHB, respectively; the difference between them is U. At this point, the relative position of the LHB and O 2p nonbonding band is directly linked with the values of U *vs.* Δ. There are three situations. When $U \ll \Delta$, corresponding to the case of strong ionic M–O bonds, the LHB is far above the O 2p nonbonding band (which is closer to the Fermi level) from which electrons are exchanged. This is the case of classical one-band cationic redox (Fig. 1c). For $U \gg \Delta$, the system is highly correlated and the O 2p nonbonding band is located closer to the Fermi level than the LHB. Electrons are removed from O 2p bonding upon charging, creating highly reactive $(O_2)^{n-}$ species that cannot be stabilized through M–(O_2) covalent interactions. The unstable $(O_2)^{n-}$ species may attack the electrolyte or decoordinate the TM and subsequently undergo reductive elimination to result in O_2 release.[57] This accounts for many irreversible phenomena observed in reported materials, such as the gradual disappearance of plateaus and capacity and voltage fading (Fig. 1e).[33,34,58–60]

Finally, a special case of $U/2 \approx \Delta$ leads to overlapping between the LHB and O 2p nonbonding band, which corresponds to the situation in which both the bands can provide electrons and realize dual-band redox to yield additional capacity. Under this circumstance, the removal of electrons results in a metastable degenerated Fermi level. The so-called TM-driven reduction coupling mechanism is proposed to bypass instability to achieve reversible anionic redox (Fig. 1f).[53] The reorganization of the oxygen network, similar to Jahn–Teller distortion that lowers the symmetry of the structure, splits the O 2p nonbonding band to stabilize the (O–O) peroxo-like species owing to the pivotal M–O covalent bonding.[15,51] This mechanism is inevitably accompanied with metal reduction and decrease in the O–O distances, which accounts for the commonly observed distortion of MO_6 octahedra in many reported anionic redox materials (Fig. 1d).[19,24,40,41,53,61] In this case, the M–(O_2) covalency turns out to be an absolute condition for reversible anionic redox and to prevent oxygen loss from the structure at higher states of charge. Another charge compensation mechanism is the generation of localized electron holes on O atoms that is coordinated by the metal and alkali metal ions, leading to the localization, and not the formation, of stable peroxide ${O_2}^{2-}$ species. Reversible anionic redox was verified in Li-rich NMC by means of ^{18}O-labelled *operando* mass spectroscopy, which confirmed no O_2 evolution.[34] It is noteworthy that the significant M–O bond covalency is closely related to the metal–ligand combinations. It is reasonable to assume that as compared to oxygen, sulfur is more likely to participate in the redox reaction, because sulfur is less electronegative than oxygen; further, it is easy to form highly covalent bonds between a metal and ligand to stabilize the structure.

It is conceivable to design theoretically feasible reversible anion redox materials by rationally selecting the metal–ligand combination and balancing the relative values of U and Δ. It has been proposed that compared with 4d and 5d metals, there is a deficient overlap between the M 3d and O 2p orbitals for the reduction coupling mechanism to occur.[51] Theorists have also verified this through theoretical calculations of the enthalpy of the oxygen release reaction for all the 3d, 4d, and 5d metals.[62] The results are consistent with the above conclusions that the difficulty of stabilizing oxygen holes is greater with 3d metals than those with the 4d and 5d ones. Of course, considering economic efficiency, 3d TM oxides are still worth studying, with the purpose of improving reversibility through artificial modulation.

3. Latent anionic redox electrode materials

3.1 Materials based on 3d metals

3.1.1 Mn-based layered oxides. The first type is the traditional layered oxide doped with other TMs; related research has found that they exhibit novel capacity that exceeds the theoretical value of charge compensation obtainable from TMs. The excess capacity can be ascribed to the contribution from oxygen redox.[22,63–68] It is intriguing since most of these materials are Na-deficient layered structures, and the underlying mechanism needs further exploration. $Na_xNi_yMn_{1-y}O_2$ layered oxide is a typical example, which has a flexible structure with different stacking configurations and has been extensively studied as a promising cathode material with abundant elements as well as high reversible capacity and operating voltage. Komaba and co-workers reported that O3-type $NaNi_{0.5}Mn_{0.5}O_2$ could deliver reversible specific capacity of 105–125 mA h g^{-1} in the voltage range of 2.2–3.8 V, as shown in Fig. 2(a).[64] When the upper cutoff voltage turned to 4.5 V, the capacity increased up to 185 mA h g^{-1}, which was expected to originate from the contribution of oxygen to charge compensation. However, the capacity quickly faded, which was explained by electrolyte decomposition. Ma *et al.* introduced P2-type layered $Na_{0.78}Ni_{0.23}Mn_{0.69}O_2$ and combined a series of spectroscopy tests to inquire into the charge compensation mechanism.[66] As exhibited in Fig. 2(b), the potential slope region was derived from the Ni^{2+} to Ni^{4+} redox couple, while oxygen anions participated in the redox process during the plateau in the high-voltage range, which provides additional capacity of 60 mA h g^{-1}. The oxidation of lattice oxygen occurs along with a gradient of TM oxidation state along the direction from surface to bulk and structural evolution appearing at the particle surface. In order to facilitate the reversibility of anionic

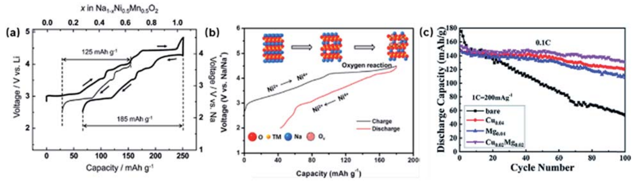

Fig. 2 (a) Initial charge–discharge curves of the sodium/$NaNi_{0.5}Mn_{0.5}O_2$ cell at the rate of 1/50C (4.8 mA g^{-1}) in the voltage ranges of 2.2–3.8 and 2.2–4.5 V *vs.* sodium metal; (b) charge compensation mechanisms in the P2-$Na_{0.78}Ni_{0.23}Mn_{0.69}O_2$ cathode; (c) cycling performance of $Na_{0.67}Mn_{0.75}Ni_{0.25}O_2$ and its doping contrast at 0.1C after 3 cycles at 0.05C.

redox and improve the cycling performance in $Na_{0.67}Mn_{0.75}Ni_{0.25}O_2$, Kong *et al.* proposed to carry out synergetic Cu and Mg codoping.[65] As shown in Fig. 2(c), the cycling stability was apparently enhanced when compared with that of the bare counterpart. The synergetic effect of Cu/Mg codoping shortens the distance between the oxygen and TMs, increasing the bonding energy and improving the anionic redox reversibility. The X-ray photoelectron spectroscopy (XPS) results revealed that the content of peroxo-like O_2^{2-} species increased after codoping; the same trend was observed with the lattice O/surface O ratio.

Another interesting strategy is to replace partial Mn with alkali metal ions.[21,23,27,69–73] As shown in Fig. 3(a), Du *et al.* studied P3-type $Na_{0.6}[Li_{0.2}Mn_{0.8}]O_2$, which exhibits a long voltage plateau at 4.1 V and splendid reversible capacity within a voltage window of 3.5–4.5 V.[21] Since the Mn redox potential is out of this voltage range, it is convenient to investigate anionic redox, which is probably the only reasonable resource for the observed capacity. The generation of holes on the O 2p bands was proven by the XPS results. The gradual fading of the plateau indicates that the oxidation of the O 2p bands is irreversible with the possibility that the holes may be stuck in the peroxide ions due to formation of an amorphous phase. Based on the above work, Rong *et al.* further explored P3-type $Na_{0.6}[Li_{0.2}Mn_{0.8}]O_2$ to gain an insight into the role of oxygen in the redox process by means of X-ray and neutron total scattering, as shown in Fig. 4(a) and (b).[71] The interlayer O–O distance was directly detected by the neutron pair distribution function (PDF) technique and was effectively matching with the peroxo-like O–O dimer (~2.5 Å), which experimentally validated the existence of O–O pairs associated with oxygen redox. The total scattering data were also refined to determine the structure of the desodiated samples. The refined result that states that the oxygen site occupation is almost unity indicates marginal structural oxygen loss, confirming that $Na_{0.6}[Li_{0.2}Mn_{0.8}]O_2$ has superior structural stability toward the oxidized oxygen ions, which is different from that in Li-rich compounds. Rather than the earlier reductive coupling mechanism, crystal structural factors were proposed as the key to stabilizing the peroxo-like species since the covalency of Mn(3d)–O(2p) is not as strong as that of M(4d,5d)–O(2p). As compared to the O-type structure, the P-type structure has longer interlayer distance due to the relatively large-sized triangular prism of the Na site, ensuring sufficient free space to achieve O–O dimerization. In order to improve the electrochemical performance, Rong *et al.* later reported P2-type $Na_{0.72}[Li_{0.24}Mn_{0.76}]O_2$ with higher sodium content and broader voltage range, which exhibited extraordinary energy density (~700 W h kg^{-1}, ~270 mA h g^{-1}, 1.5–4.5 V) attributable to both Mn^{3+}/Mn^{4+} redox and oxygen redox.[72] The minimal volume change in the global P2 structure was found after the complete deintercalation of Na^+ ions, which could be attributed to the excellent structural stability. The interslab distances determined from the *in situ* XRD change by a small degree during Na deintercalation because the electrons are removed from the oxidation of oxygen, reducing the repulsive force between the O 2p orbitals, which is below the activation energy needed for slab glide. It was revealed that anionic redox could stabilize the structure in addition to its already known advantage of increasing the capacity. The shortening of the length of the anionic redox plateau was attributed to the possible side reactions between the unstable oxidized species and electrolytes in the high-voltage window. High-capacity

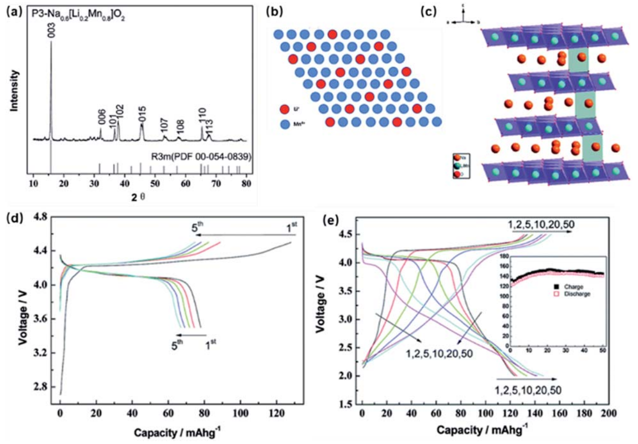

Fig. 3 Crystal structure of $Na_{0.6}[Li0._{2}Mn_{0.8}]O_2$: (a) XRD pattern; (b) ordered Li/Mn atoms; (c) P3 layered structure. Charge–discharge profiles and cycling stability of P3-$Na_{0.6}(Li_{0.2}Mn_{0.8})O_2$; (d) 10 mA g^{-1} between 3.5 and 4.5 V; (e) 15 mA g^{-1} between 2 and 4.5 V.

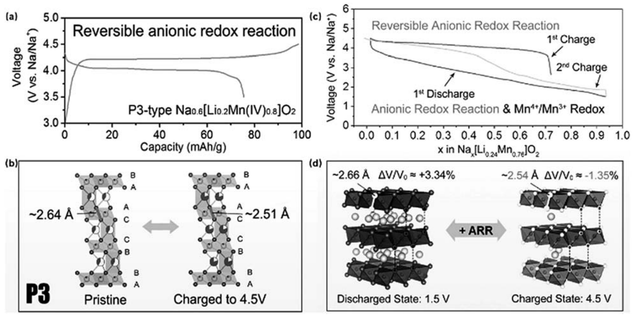

Fig. 4 (a) Charge–discharge curves of P3-$Na_{0.6}[Li_{0.2}Mn_{0.8}]O_2$; (b) illustration of structural evolution during desodiation, with the emergence of a short O–O pair (2.5 Å) in the charged sample; (c) charge–discharge curves of P2-$Na_{0.72}[Li_{0.24}Mn_{0.76}]O_2$; (d) schematic diagram of the volume change during cycling, with interlayer O–O distances explicitly marked.

$Na(Li_{1/3}Mn_{2/3})O_2$ was reported by Kim *et al.*, which was systematically designed by first-principles calculations.[73] The Li/Na mixing enthalpy was presented as a function considering the substitution preference of Na in the Li counterpart Li_2MnO_3. The PDOS demonstrated that a portion of the O 2p orbitals was above the Mn 3d orbital. Therefore, the predicted unhybridized states (O 2p nonbonding band) verify the oxygen redox activity, as shown in Fig. 5(a)–(d). In Fig. 5(e)–(h), the spatial electron distribution (SED) shows that the presence of the isolated electron densities of the O 2p orbitals exhibits the characteristics of oxygen lone pairs with a linear shape along the Na–O–Li direction, similar to the Li–O–Li configuration observed in the same energy range earlier. During desodiation, the change in the electron density of the O 2p orbitals around the vacancy implies that the labile Na–O–Li participates in charge compensation. Yabuuchi *et al.* prepared P2-type $Na_{5/6}[Li_{1/4}Mn_{3/4}]O_2$ and utilized the ion-exchange method to synthesize its O_2-type counterpart $Li_x[Li_{1/4}Mn_{3/4}]O_2$ with glided TM layers and maintaining the in-plane cation ordering.[27] The electrode performances were determined and compared for both Na- and Li-based systems. Both the samples deliver large reversible capacity of around 200 mA h g^{-1}, regardless of the difference in the charge carriers. A structural analysis indicates that in-plane reorganizations occur in both the samples, presumably due to the irreversible oxygen loss during the first charge, which consequently influences the subsequent cycling performance.

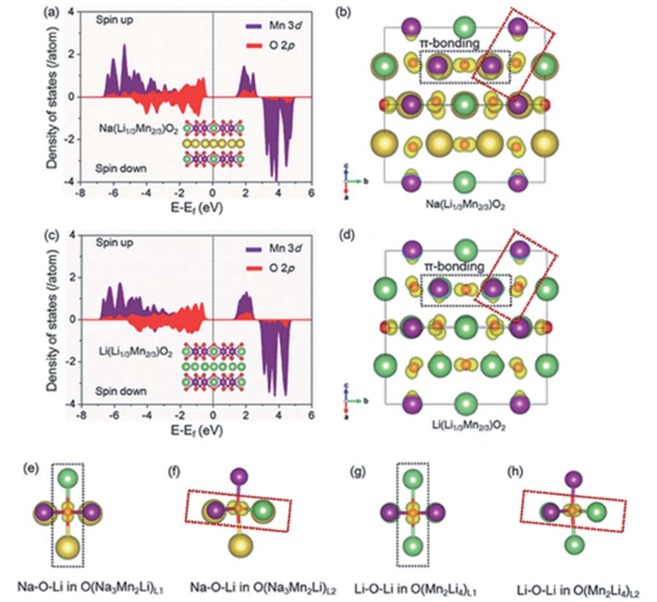

Fig. 5 Electronic structures in $Na(Li_{1/3}Mn_{2/3})O_2$ and $Li(Li_{1/3}Mn_{2/3})O_2$. (a) and (c) Combined graphs of the partial densities of states (PDOSs) of Mn 3d orbital electrons (purple) and O 2p orbital electrons (red) in the fully sodiated $Na(Li_{1/3}Mn_{2/3})O_2$ and fully lithiated $Li(Li_{1/3}Mn_{2/3})O_2$, respectively. The PDOS of Mn in both the oxides exhibits d_{xy}, d_{yz}, and d_{xz} orbitals in the t_{2g} band (spin-up electrons, $t_{2g}{}^3$). Spatial electron distribution in the occupied band from −8 to −2 eV for (b) $Na(Li_{1/3}Mn_{2/3})O_2$ and (d) $Li(Li_{1/3}Mn_{2/3})O_2$. Local spatial electron distribution in the occupied band from −2 to 0 eV (Fermi level) for the two kinds: (e) O in the black circle and (f) O in the red circle from Fig. 5(b) of the O coordinated by three Na, two Mn, and one Li in the structure of $Na(Li_{1/3}Mn_{2/3})O_2$, and the distribution in the same range for the two Os: (g) O in black circle and (h) O in red circle from Fig. 5(d) of O surrounded by four Li and two Mn in the structure of $Li(Li_{1/3}Mn_{2/3})O_2$.

The alkali metal ions are not the only requisite to trigger anionic redox.[26,44,45,74] Yabuuchi and co-workers introduced P2-type $Na_{2/3}[Mg_{0.28}Mn_{0.72}]O_2$, which delivers surprisingly large reversible capacity of 220 mA h g^{-1} in Na cells, which is obviously beyond the theoretical value based on the Mn^{3+}/Mn^{4+} redox reaction (Fig. 6).[26] Anomalously large capacity is supposed to be derived from the participation of oxygen redox reactions. It was first revealed that magnesium, which is an alkaline-earth metal, is also a valid element to trigger the oxygen redox activity, which is similar to Li in Li-rich materials and its solid solutions. It is worth mentioning that the ion-exchanged counterpart is almost electrochemically inactive in Li cells, which is different from the situation mentioned above. It seems that this chemistry is uniquely observed in Na systems. The reasons for this phenomenon need further research, and new theories need to be formulated to explain them. As shown in Fig. 7, Maitra and co-workers reported that P2-type $Na_{2/3}[Mg_{0.28}Mn_{0.72}]O_2$ exhibits excess capacity. Mg and Mn are arranged in a honeycomb structure in the TM layers.[44] A range of advanced spectroscopic techniques were performed to illustrate that oxygen redox participates in charge compensation. Unlike earlier alkali-rich compounds where alkali ions were removed from both alkali and TM layers (consequently increasing the oxygen loss), it was found that $Na_{2/3}[Mg_{0.28}Mn_{0.72}]O_2$ does not lose oxygen, as per the experimental results shown in Fig. 7(c). It turned out that Mg^{2+} ions remain in $Na_{2/3}[Mg_{0.28}Mn_{0.72}]O_2$; they interact with the O 2p orbitals, suppressing the evolution of oxygen with holes on the 2p states. Bai *et al.* reported a new Na-deficient P2-$Na_{2/3}Mn_{7/9}Zn_{2/9}O_2$ phase by doping an element (Zn) more electronegative than Mg.[45] This material exhibited reversible capacity of around 200 mA h g^{-1} in Na half-cells. The XPS results reveal the electronic state evolutions of Mn and O (as shown in Fig. 8), showing the emergence of peroxo-like species in the charged sample along with the Mn redox reaction. The oxidized species can be stabled with no O_2 release. The fading capacity can be ascribed to the evident cationic migration. Density functional theory (DFT) calculations reveal the existence of an oxygen nonbonding state close to the Fermi level, which activates the oxygen redox reaction in this material.

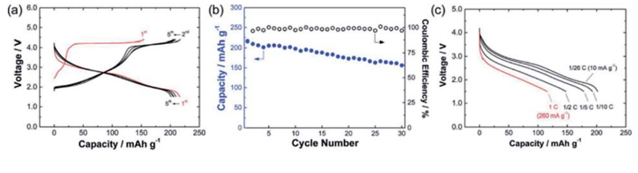

Fig. 6 Electrochemical characterization of $Na_{2/3}[Mg_{0.28}Mn_{0.72}]O_2$ in Na cells; (a) charge–discharge curves of the $Na/Na_{2/3}[Mg_{0.28}Mn_{0.72}]O_2$ cell cycled at the rate of 10 mA g^{-1} in the voltage range of 1.5–4.4 V. Discharge capacity and coulombic efficiency of the cell are plotted in (b). (c) Rate capability of the $Na/Na_{2/3}[Mg_{0.28}Mn_{0.72}]O_2$ cell. The cell was charged at the rate of 10 mA g^{-1} to 4.4 V and then discharged to 1.5 V at different current densities. Sample loading values for the electrodes used are (a), (b) 2.2 and (c) 3.2 mg cm^{-2}.

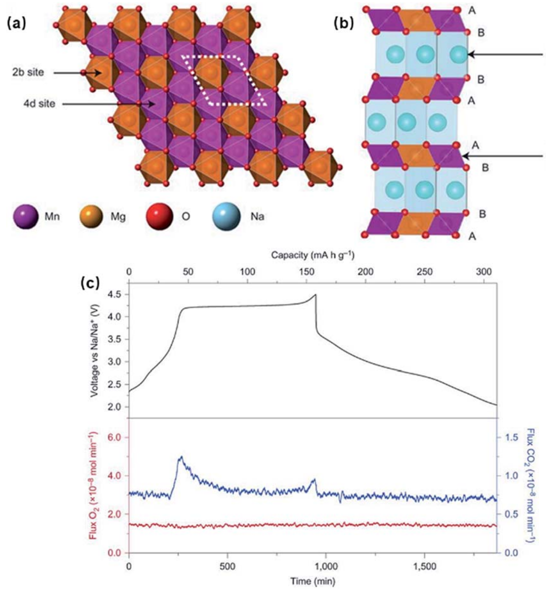

Fig. 7 (a) In-plane honeycomb ordering in the TM layer where the Mg sits in the center of the honeycomb surrounded by Mn ions; (b) schematic of the P2 structure that shows the stacking sequence of the MO_2 layers; (c) gas loss of $Na_{2/3}[Mg_{0.28}Mn_{0.72}]O_2$ during electrochemical (de)sodiation. The top panel shows the electrochemical response of the cell and the bottom panel shows the O_2 and CO_2 gases evolved as a function of the state of charge.

Besides substituting A for M, introducing TM vacancies is another possible approach for introducing anionic redox.[66,75] The oxygen lone pairs can be generated along the direction of A–O–□ and □–O–□ (□: TM vacancy). Ma and co-workers introduced a novel layered oxide $Na_{0.78}[\square_{0.08}Ni_{0.23}Mn_{0.69}]O_2$, wherein an apparently excess capacity was obtained over the first charge.[66] Based on the results of various spectroscopic techniques, the gradients of the TM oxidation state are linked to the redox of the lattice oxygen at the surface of the particles. In the P2 structure, AA stacking leads to larger interlayer repulsion. It is more likely that oxygen vacancies form over the high-voltage plateau, with irreversible structural decomposition during the first cycle. Recently, $Na_2Mn_3O_7$ or $Na_{4/7}[\square_{1/7}Mn_{6/7}]O_2$ (□: Mn vacancy) has attracted increased interest.[46,47,76,77] As shown in Fig. 9(b), $Na_2Mn_3O_7$ has a triclinic structure composed of Na^+ and $[\square_{1/7}Mn_{6/7}{}^{4+}]$ layers that are alternately stacked. The configuration of □–Mn ordering in the $[\square_{1/7}Mn_{6/7}{}^{4+}]$ layer represents a $\sqrt{7} \times \sqrt{7}$ superlattice.[78,79] Boisse *et al.* reported that $Na_{2-x}Mn_3O_7$ can operate as a reversible cathode with a high average voltage of 4.1 V.[46] As shown in Fig. 9(c), owing to the redox activity of both Mn and O, $Na_2Mn_3O_7$ delivers large reversible capacity of about 200 mA h g^{-1} within the voltage window between 1.5 V and 4.7 V. When compared with previous literature demonstrating the electrochemical reaction based on Mn^{4+}/Mn^{3+} when the upper cutoff voltage is 3.0 V, excess reversible capacity of about 75 mA h g^{-1} is obtained within the range of 3.0–4.7 V, corresponding to 1.0 Na^+ removal per formula unit. The combination of theoretical calculations and experimental results validated the presence of oxygen lone pairs

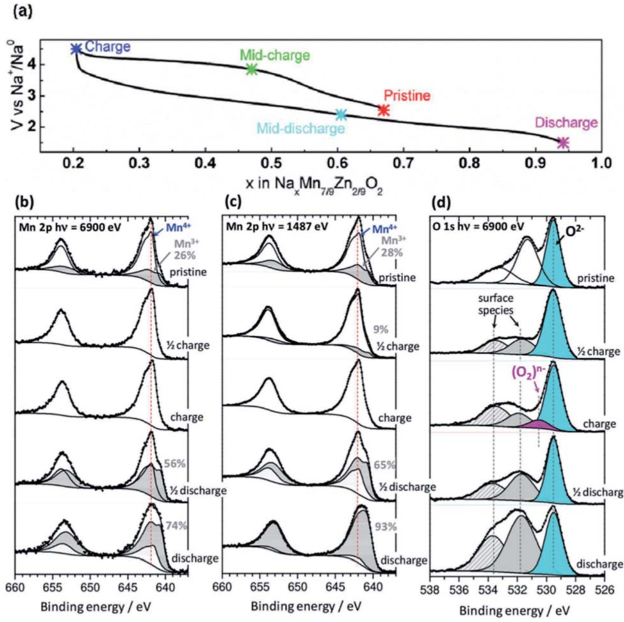

Fig. 8 (a) Galvanostatic charge–discharge curve showing the representative points at which the *ex situ* samples were collected for HAXPES and XPS analysis. (b) HAXPES Mn(2p), (c) XPS Mn(2p), and (d) HAXPES O(1s) spectra of the samples upon the first cycle. HAXPES data were recorded with 6.9 keV photon energy and XPS data with 1487 eV. All the Mn(2p) spectra were fitted with the $NaMnO_2$ reference (grey curve), except for the XPS spectrum of the discharged sample.

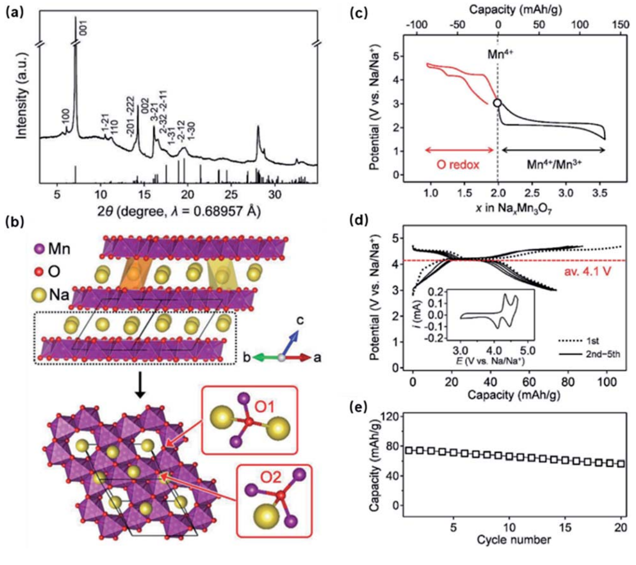

Fig. 9 (a) Synchrotron X-ray diffraction pattern of $Na_2Mn_3O_7$ with black bars indicating the simulated diffraction peaks. (b) Crystal structure of $Na_2Mn_3O_7$. O coordinated by two Mn is labeled as O1, whereas O coordinated by three Mn is labeled as O2. Mn vacancies exist in the Mn layers. (c) Potential profile (second cycle) of $Na_2Mn_3O_7$ upon (de)sodiation between 1.5 and 4.7 V *versus* Na/Na^+. The dashed grey box indicates the high-voltage region where O is involved in the active redox process. (d) Galvanostatic charge–discharge curves between 3.0 and 4.7 V *versus* Na/Na^+, and (e) cycling stability of the oxygen redox region of $Na_2Mn_3O_7$ between 3.0 and 4.7 V at the rate of C/20. The inset shows a cyclic voltammetry curve at the second cycle at a scan rate of 0.1 mV s^{-1}.

close to the Mn vacancies. Oxygen redox reactions contribute to the capacity and Mn–O bonds maintain stability during cycling. The capacity retention was up to 85% after 20 cycles, as shown in Fig. 9(e). The unchanged distance between the TM layers along with the consistently sharp diffraction peaks verify the stable layered structure. This can be attributed to the coulombic interaction between the Mn vacancies and Na^+ ions. Li *et al.* performed synchrotron X-ray absorption near edge structure (XANES) along with XPS to comprehensively investigate the charge compensation in $Na_2Mn_3O_7$.[47] It turned out that the Mn^{3+}/Mn^{4+} redox reaction and oxygen redox occur separately during cycling. The vacancies in the TM layer lead to uneven bond lengths. When compared with alkali-rich materials, the removal of Na^+ is less, which means that oxygen does not have to provide too many electrons; this facilitates the high reversibility of anionic redox.

3.1.2 $NaFeO_2$.

α-$NaFeO_2$ has a typical O3-type structure appearing in many layered electrode materials.[10,80–83] Layered $Na_xFe_yM_{1-y}O_2$ (M for Mn, Ni, *etc.*) has been extensively studied and is one of the most promising cathode materials for SIBs.[84,85] However, the poor cycling performance has always been a common issue, and its underlying principle remains unclear. Yabuuchi *et al.* reported that O3-type $NaFeO_2$ exhibits reversible capacity of 80–100 mA h g^{-1} with a nearly flat voltage plateau at around 3.3 V, as shown in Fig. 10(a).[80] Fig. 10(b) shows that acceptable cyclability is limited in the composition of $x = 0$–0.45 and considerably depends on the cutoff voltage since the electrode performance is rapidly deteriorated when $x > 0.5$ in $Na_{1-x}FeO_2$. This phenomenon could be ascribed to the irreversible structural changes due to iron ion migration in the layered host structures.

Recently, Chen *et al.* reported that apart from Fe^{3+}/Fe^{4+} redox, oxygen redox contributes toward providing capacity in O3-type $NaFeO_2$, but at different periods of the Na removal process, based on the XPS and soft X-ray absorption spectroscopy (XAS) data.[82] The density of states (DOS) results demonstrate that the Fe 3d and O 2p orbitals are highly overlapped when neighboring the Fermi level, both providing electrons upon charging. As shown in Fig. 10(c) and (d), Fe migration from the TM layer to the Na layer was directly observed at the atomic scale, which blocked Na ion diffusion, leading to rapid performance fading in $NaFeO_2$. Susanto and co-workers proposed that charge compensation cannot be realized through cationic redox upon Na removal based on the invariable Fe K-edge of the *in situ* XAS results, as shown in Fig. 10(e).[81] Oxygen redox reaction is proven to be predominantly responsible for charge compensation, as validated by the *ex situ* XANES data. It is revealed that $NaFeO_2$ irreversibility is due to oxygen release and the formation of Fe_3O_4 observed by transmission electron microscopy (TEM); these hamper Na insertion back into the structure upon discharging. Gao *et al.* gained an insight into ion transport and O 2p electrons in $NaFeO_2$ through first-principles calculations.[83] It was discovered that the lattice strain can influence the diffusion barrier of ions and the stability of oxygen. Therefore, it is possible to combine both tension and compression *via* a reasonable design to facilitate Na (de)intercalation and enhance the electrochemical performance.

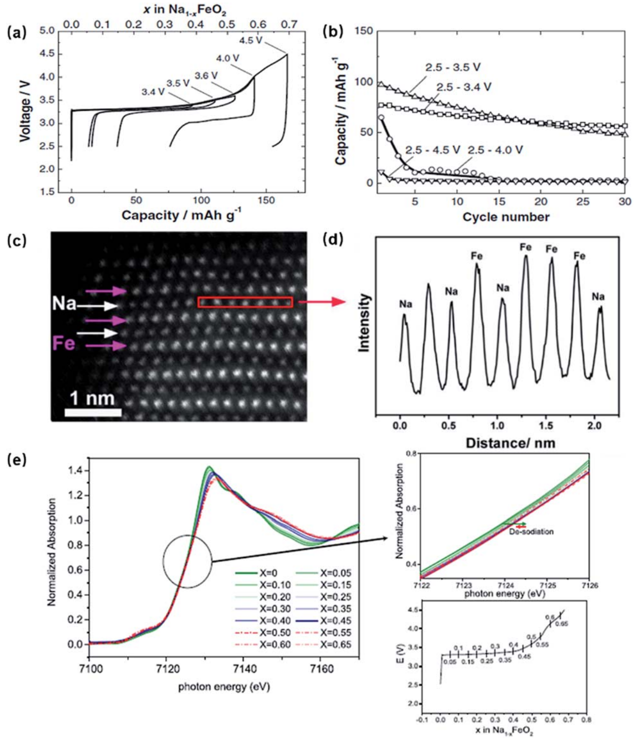

Fig. 10 (a) Initial charge–discharge curves of Na/$NaFeO_2$ cells with different cutoff voltages at the rate of 12 mA g^{-1}. (b) Discharge capacity retention for 30 cycles with different cutoff voltages at the rate of 12 mA g^{-1}. (c) HAADF images of $NaFeO_2$ in the fully charged state. (d) Corresponding line profile acquired from the red rectangular region marked in (c). (e) Normalized Fe K-edge *in situ* XAS spectra of $Na_{1-x}FeO_2$ obtained in the transmission mode as compared to those from the reference materials. Insets show the enlarged spectra of the Fe K-edge and charging curve of $Na_{1-x}FeO_2$ with measurement points for the Fe K-edge spectra in the sodium intercalation process, respectively.

3.1.3 $NaSeO_2$.

Su *et al.*, for the first time, reported the Na-rich Na_2SeO_3 material with a monoclinic layered structure to be a promising cathode material for SIBs.[86] Na_2SeO_3 is composed of NaO_6 octahedron and SeO_3 pyramids joined together at the edges. The oxygen atoms are located at three different sites coordinated with one Se and various amounts of Na atoms (3, 4, and 5). This structural configuration can provide a flexible environment for oxygen to rotate and form peroxo-like dimers with the adjacent ones. This material mixed with a conductive agent can deliver discharge capacity of 232 mA h g^{-1} after the activation process of charging up to 4.7 V with a long plateau at around 4.5 V. The discharge capacity reaches the maximum in the second cycle and then gradually decays with the fading of the initial charging plateau and decreasing the operating potential. The XPS results reveal that the electronic state of selenium remains unchanged during the charging process, which suggests that oxygen redox contributes to the charge transfer. The theoretical calculations exhibit that the energy band of oxygen is above that of selenium and is closer to the Fermi level. This validates the involvement of anionic redox and partially explains the poor cycling performance since there is deficient band overlap to stabilize the oxidized species when charging.

3.1.4 $NaCrS_2$. The prevailing strategies for designing high-capacity positive electrodes are mostly concentrated on the advanced TM redox and the introduction of oxygen redox activity. Shadike and co-workers reported sole reversible sulfur redox in layered O3-type $NaCrS_2$.[87] As shown in Fig. 11(a), during the initial charge, the $NaCrS_2$ electrode exhibits high capacity of 95 mA h g^{-1} (0.49 Na^+ per $NaCrS_2$) at a flat voltage of 2.85 V. This capacity is much larger than that observed in $LiCrS_2$ (30 mA h g^{-1}). The first discharge capacity is 92 mA h g^{-1} with a discharge curve comprising a slope between 2.1 and 2.8 V prior to the plateau at 2.0 V. In Fig. 11(b), the capacities gradually increase during the first three cycles due to the activation process and keep decreasing thereafter down to 78.5 mA h g^{-1} after 100 cycles. The coulombic efficiency increases with the number of cycles and reaches almost 100%. Based on the XANES results for Cr and S (shown in Fig. 11(c) and (d), respectively), rather than chromium, sulfur was discovered to be electrochemically active, contributing toward charge compensation through the redox of $S^{2-}/S_2^{\ 2-}$. It is impressive that there is a marginal change in the lattice parameter *c* during the desodiation and sodiation processes, which can be explained by the existence of chromium/sodium vacancy antisites. DFT calculations reveal that the unique band structure of the S 3p orbitals is responsible for the sulfur redox reaction in $NaCrS_2$ and holes generated on the sulfur 3p band condense and stabilize *via* the formation of dimer $S_2^{\ 2-}$.

3.2 Materials based on 4d metals

3.2.1 Ruthenium-based layered oxides. Although layered Na_xMO_2 has been intensively analyzed as a cathode material for SIBs, the electrochemical properties of layered Na_2MO_3, whose lithium analogues exhibit extraordinary performance, have not been clarified until now. Tamaru *et al.* reported that O3-type Na_2RuO_3 synthesized by a conventional solid-state reaction yields initial discharge capacity of 147 mA h g^{-1} in accordance with the theoretical value calculated from the Ru^{5+}/Ru^{4+} redox.[88] The *ex situ* XRD results show that the compositional region of the two-phase state in $Na_{2-x}RuO_3$ is different from that in $Li_{2-x}RuO_3$.[40] It was presumed that the ordered $[Li_{1/3}Ru_{2/3}O_2]$ layers lead to strong interlayer interaction, which stabilizes the ordered intermediate states in $Li_{2-x}RuO_3$, arousing the phase separation for wider compositional ranges.[89] However, the interlayer interaction in Na_2RuO_3 is too weak to form a stable intermediate state due to the absence of cationic ordering in the TM slabs. Based on the above work, Boisse and co-workers synthesized a new type of Na_2RuO_3 with a honeycomb-type cation arrangement in the $[Na_{1/3}Ru_{2/3}O_2]$ slabs, as shown in Fig. 12(a), by a thermal decomposition method.[24,90] As shown in Fig. 12(b)–(d), the two polymorphs of Na_2RuO_3 exhibit distinct electrochemical performance because of which ordered Na_2RuO_3 delivers capacity of 180 mA h g^{-1}, corresponding to 1.3 Na^+ removal, which is beyond that of the single-electron cationic redox reaction as shown by disordered Na_2RuO_3 (140 mA h g^{-1}). As compared to the S-shaped electrochemical curve of disordered Na_2RuO_3, ordered Na_xRuO_3 ($0.7 < x < 2$) exhibits a staircase-type charging curve with one plateau at around 2.5 V and another one located at 3.6 V; the latter is associated with the excess capacity originating from the oxygen redox process. Distinct from the O3–P3 phase transition in disordered Na_xRuO_3, an ordered intermediate phase X occurs at

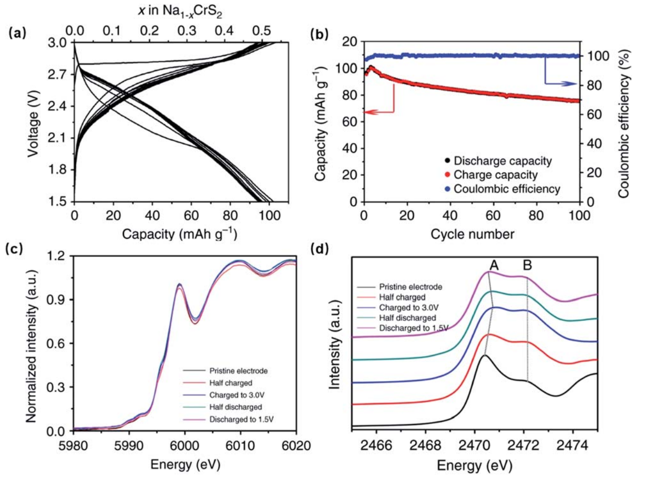

Fig. 11 (a) Galvanostatic charge–discharge curves, (b) cyclic performances, and coulombic efficiencies of $NaCrS_2$ electrode at 0.5C. (c) Cr K-edge XANES spectra of $NaCrS_2$ electrodes at various states. (d) S K-edge XANES spectra of $NaCrS_2$ at the initial cycle.

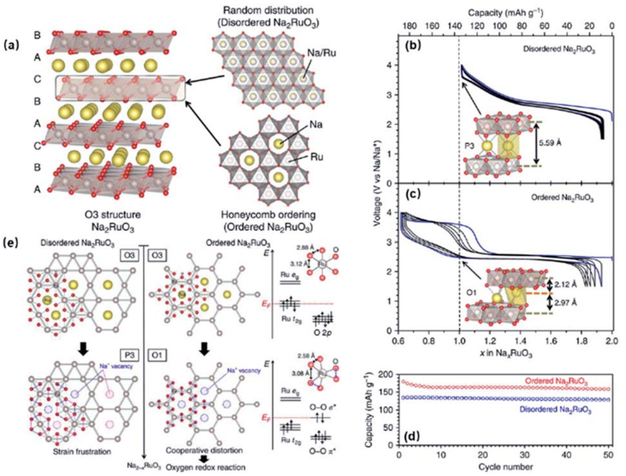

Fig. 12 (a) Structure of ordered and disordered Na_2RuO_3. Oxide ions (red) stack in the manner of ABCABC, while both Na (yellow) and Ru (grey) occupy octahedral sites for both Na_2RuO_3. Ordered Na_2RuO_3 has honeycomb-type cation ordering in the $[Na_{1/3}Ru_{2/3}]O_2$ slab. Disordered Na_2RuO_3 has a randomly distributed $[Na_{1/3}Ru_{2/3}]O_2$ slab. Galvanostatic cycling curves recorded at 30 mA g^{-1} for (b) disordered and (c) ordered Na_2RuO_3 with the first cycle highlighted in blue. Insets show the coordination environment of Na at $x = 1.0$ for each phase. (d) Capacity retentions for disordered (blue squares) and ordered (red circles) Na_2RuO_3. (e) Schematic representation of the structural changes during charge–discharge for disordered Na_2RuO_3 and ordered Na_2RuO_3.

the first plateau and O1 phase is formed in ordered Na_1RuO_3. Importantly, as shown in Fig. 12(e), the O–O distance is shortened due to distortion in the RuO_6 octahedron, which brings the energy level of the O–O antibonding σ* band closer to the Fermi level, triggering anionic redox activity. Further, this marginally differs in the mechanism sequence from earlier theories. The honeycomb-type cation ordering is demonstrated as the essential condition to induce excess capacity in Na-rich layered oxides. When compared with 3d TMs, the covalent bond between the peroxo-like species $(O_2)^{n-}$ 2p and Ru 4d orbitals is stronger, which facilitates structural integrity and restrains oxygen gas release. Rozier *et al.* reported Na-rich layered $Na_2Ru_{1-y}Sn_yO_3$ with different doping rates ($0 < y < 1$).[91] As y increases, particularly when $y > 0.25$, the 3 original consecutive platforms are reduced to only 2, and the subsequent curves convert into an S shape as the capacity loss increases during the first discharge. All the samples deliver large capacity exceeding that of the single-band redox of Ru^{4+}/Ru^{5+}; a dual cationic–anionic redox process was proposed based on the XPS analysis. The capacity decay could be attributed to the cation disordering and fading of crystallinity. The structural evolution in $Na_2Ru_{1-y}Sn_yO_3$ goes through a solid solution prior to two-phase evolution and returns to a solid solution, differing from that observed in Li analogues, presumably due to the differences in the sizes and polarities of Na^+ and Li^+.

Qiao and co-workers originally introduced Na_3RuO_4 (Ru^{5+}) or $Na[Na_{1/2}Ru_{1/2}]O_2$ as a pure Na-rich layered oxide cathode prototype for SIBs, which exhibits partially reversible capacity originated only from the contribution of the anionic redox reaction.[92] Advanced *in situ* Raman spectroscopy was performed to provide systematic information on oxygen-based anionic redox behaviors. Otoyama *et al.* reported that 3 Na can be removed from Na_3RuO_4 with 1 electron compensated from the Ru^{5+}/Ru^{6+} redox and then the remaining charge could be derived from the oxygen redox.[93] This is unanticipated since Ru is seldom oxidized to such a high valence in LIBs. Fig. 13(a) shows the voltage–composition profile for a Na_3RuO_4/Na half-cell. The initial charge curve exhibits a staircase-type structure with 3 successive plateaus located at 3, 3.5, and 4.6 V, corresponding to the extraction of 1, 2, and 3 Na, respectively. The discharge profile demonstrates a rapid potential drop and subsequent S-type curve. The extracted Na (3) is almost entirely reinserted back into the bulk upon discharging, but the material shows relatively poor cycling performance, as shown in Fig. 13(d). In addition, cycling with different degrees of charges (Fig. 13(b) and (c)) shows distinct capacity retentions, which reveals that charging to a higher voltage can inevitably lead to irreversibility. DFT calculations reveal that for A_xRuO_4, as the radius of the alkali metal increases, the coordination of Ru decreases, tending toward a higher oxidation state for stabilization.

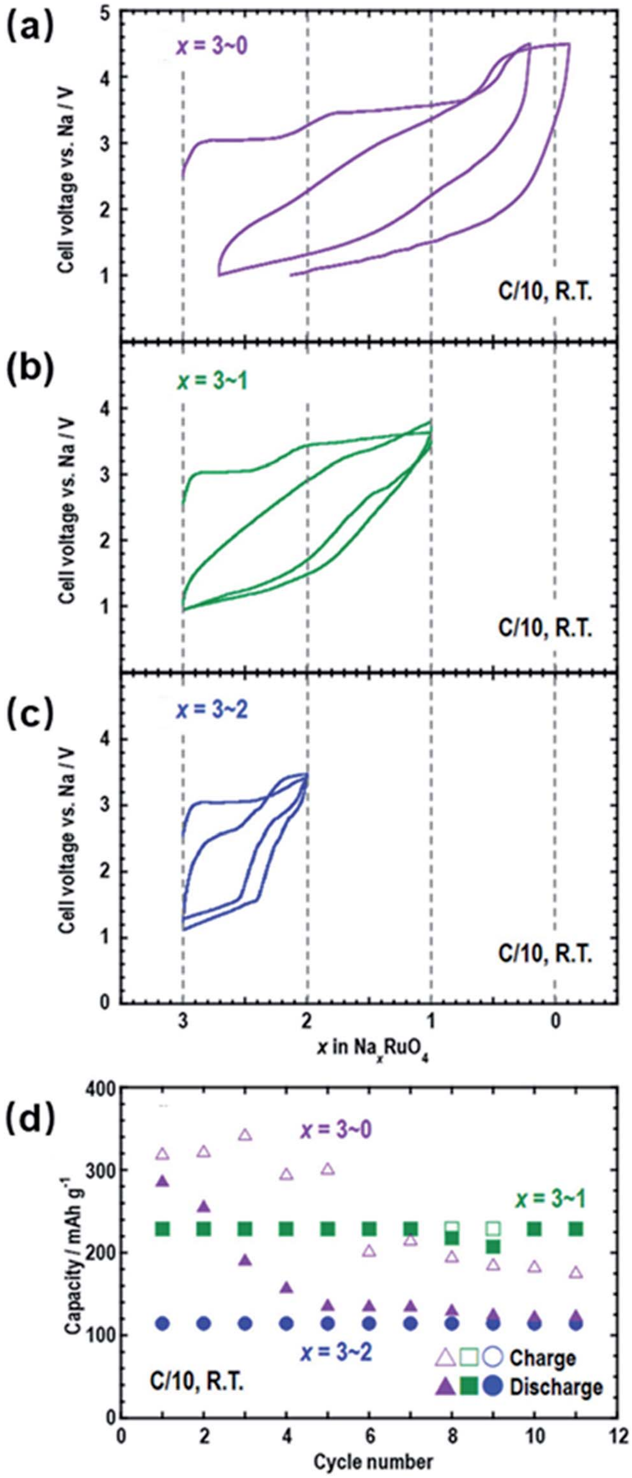

Fig. 13 First and second galvanostatic curves of the Na cells with Na_xRuO_4 between (a) $x = 3–0$, (b) 3–1, and (c) 3–2. The cells were operated at room temperature at C/10 rate and cutoff voltage of ≈0.5 V. (d) Cycling performance of the cells with $x = 3–0$ (purple triangle), $x = 3–1$ (green square), and $x = 3–2$ (blue circle) in Na_xRuO_4.

3.3 Materials based on 5d metals

3.3.1 Iridium-based layered oxides. Perez and co-workers reported the electrochemical performance of Na-rich O3-type Na_2IrO_3, which can (de)intercalate 1.5 Na^+ with no indication of oxygen gas release or cation migrations.[25] As shown in Fig. 14(b), the first charge curve goes through two plateaus located at 2.7 V and 3.7 V, with a subsequent discharge capacity of 130 mA h g^{-1}. It is worth mentioning that unlike previous anionic redox materials, both these plateaus are consistently maintained during cycling. When charged up to $Na_{0.5}IrO_3$, the O3 structure turns into the O1 structure, with O1′ as the intermediate phase, as shown in Fig. 14(c). Such large capacities are experimentally testified to arise from the accumulated mixed cationic–anionic redox reaction; further, anionic redox is proven to be active at the early stages of the Na extraction process. From the inset of Fig. 14(a), it is evident that pristine Na_2IrO_3 comprises slightly distorted IrO_6 octahedra (like Li_2IrO_3), which raises an open question: whether this distortion is the key condition for the early activation of anionic redox activity.[19] Further investigations need to be carried out. Zhang *et al.* reported O3-type Na-rich $Na_{1.2}Mn_{0.4}Ir_{0.4}O_2$, which involves both cationic and anionic contributions during the redox process.[94] During the first charge process, $Na_{1.2}Mn_{0.4}Ir_{0.4}O_2$ exhibits capacity of around 180 mA h g^{-1}, with 68 mA h g^{-1} originating from Mn redox and 0.6 Na removal due to oxygen redox. From the DFT calculations, the strong covalent Ir–O bonding can stabilize the electrons on the oxygen holes and hinder O_2 release.

4. Challenges and possible solutions

Although several materials have been reported to deliver extremely high capacities through anionic redox reactions, ubiquitous irreversibility leads to rapid degradation of performance, including plateau disappearance as well as capacity and potential decays, which hinder the practical applications of anionic redox.[59,72,81,95,96] In terms of the basic mechanism of anion redox, irreversibility originates from the lack of continuous covalent bonding between the metastable peroxo-like species and TMs, which may induce a series of consequences, including O_2 release, TM migration, side reactions with the electrolyte, *etc.*[60,71,82] Moreover, when compared with the integral crystal structures of the electrode materials for LIBs, the counterparts in SIBs tend to have crystal defects since sodium deficiency is relatively common. The desodiation process is often accompanied by complicated phase transition and structural evolution, which leads to irreversibility. Doublet's group demonstrated the schematic galvanostatic curves of A-rich TM oxides to illustrate the cationic and anionic redox processes for four different scenarios.[52] Firstly, under the ideal condition of completely reversible and distinct cationic and anionic redox reactions with no cation migration and no O_2 release, the voltage profile exhibits highly reversible electrochemistry with two persistent plateaus corresponding to $M^{n+}/M^{(n+1)+}$ and $O^{2-}/(O–O)^{n-}$. When metastable peroxo-like species decoordinate from the metallic network accompanied by cation migration or disorder, the redox is not reversible and the capacity displayed during charging cannot be completely retained during discharging, leading to continuous hysteresis and an S-shape profile as a result of the multiplication of TM and oxygen redox centers. This is the most common case among the recently reported materials. There is another special case in which the plateaus during charging can be retained during cycling on the basis of no O_2 release at higher potential and fully reversible cationic migration. The TM reduction induced during charging can motivate a cationic redox couple upon discharging, prior to anionic redox, resulting in a sloped discharge curve. Lastly, capacity decay due to oxygen loss during charging is partially recovered during discharging by the introduction of a dominant TM redox with irreversible cationic migration and electrolyte decomposition. The process is accompanied by persistent decomposition of the electrode, yielding continuous voltage hysteresis and capacity fading (Fig. 15).

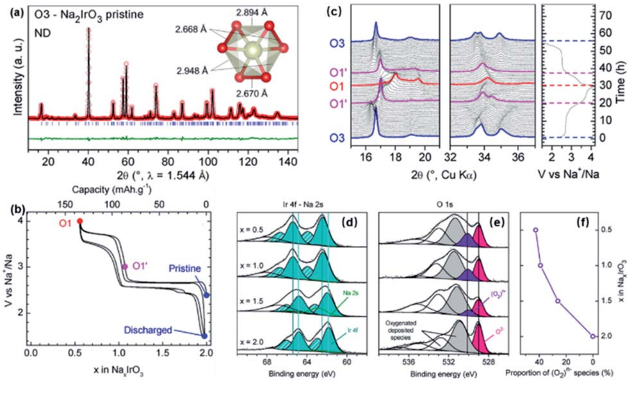

Fig. 14 (a) Refinement in neutron diffraction patterns for pristine Na_2IrO_3. Inset shows the different O–O distances around the Ir atoms obtained from neutron diffraction. (b) First and second galvanostatic cycles of Na_2IrO_3 *vs.* Na. (c) *In situ* XRD study of Na_2IrO_3 (cycled at C/20 between 1.5 and 4.3 V). Pristine O3, O1′, and O1 phases are highlighted in blue, pink, and red, respectively. XPS analyses of Ir 4f (d) and O 1s (e) peaks show that both Ir and oxygen are oxidized on the first plateau, and oxygen is only oxidized on the second plateau. The proportion of $(O_2)^{n-}$ species depending on the state of charge is shown in (f).

In order to improve the reversibility of the anionic redox materials, some possible solutions are proposed. Based on the differences in the orbitals of the abovementioned 3d, 4d, and 5d metals, it is feasible to mix 3d metals with 4d or 5d metals to obtain additional orbital overlaps, leading to better material stability, as recently reported.[15,42,91,94] In addition to the configurations reported so far, it is innovative to explore other configurations to induce nonbonding O 2p bands (Fig. 16). Another possible way is by increasing the M′/M ratio ($A_x[M'_yM_{1-y}]O_2$) to impede cationic migrations.[92,93,97] Intersite migration of TMs can also be suppressed with regard to heavier or larger-sized metals due to incompatibility with the tetrahedral site, as shown in Na_2RuO_3 by Yamada's group.[24] It is promising to design a stable host structure that undergoes fewer phase changes and less stress during cycling. Enthalpy as a function of x content is widely regarded as a tool to determine the ideal rate of contents to improve reversibility. The controllable replacement of partial oxygen with sulfur can increase M(nd)–L(np) overlaps to induce the reductive coupling mechanism, thereby enhancing the structural stability. It is promising to design double-anion systems.[87,98] It is noteworthy that theoretical calculations are useful tools to provide valid supporting information for anionic redox. On the basis of first-principles DFT calculations, crystal orbital overlap population (COOP) and DOS

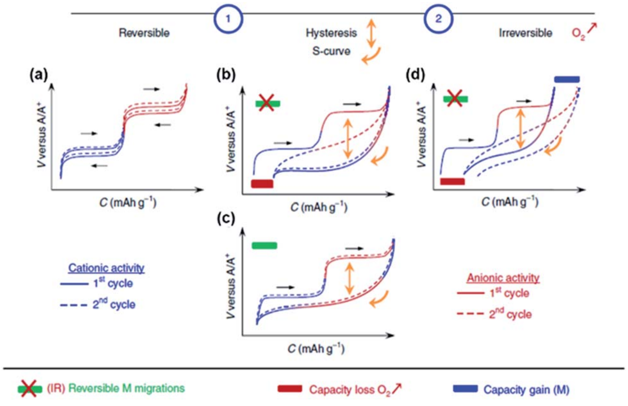

Fig. 15 Schematic galvanostatic curves of A-rich-TMOs for different scenarios. (a) Fully reversible cationic and anionic processes with no O_2 release and no cation migration in charge. (b–d) First part of the discharge corresponds to cationic activity due to O_2 release at high charging. This leads to hysteresis between charge–discharge. (b) When O_2 gas is released in the first charge due to cationic migration/disorder, the process becomes irreversible, leading to persistent hysteresis in subsequent cycles and an S-shape curve due to the multiplication of TM and (O–O) redox centers. (c) Plateaus during charging are recovered if no O_2 release occurs at high charging and if cationic migrations are fully reversible during discharging. (d) Capacity loss during charging due to O_2 gas release can be partially compensated during discharging by the activation of a novel TM redox couple.

can be utilized as a beneficial tool to evaluate the contribution of O band to the redox activity and predict the extent to which it interacts with the TM orbitals to stabilize the peroxo-like species.[73,99] The direction of theoretical calculations can be further developed in future research to assist scholars in the design of favorable materials with reversible anionic redox. Finally, considering that the voltage plateau of anionic redox in SIBs is up to around 4.2 V, it is necessary to take the electrolyte into account and develop well-matched electrolytes to facilitate interfacial stability.

It should be pointed out that the present theories involving anion redox are based on the reported materials for LIBs. Although lithium and sodium belong to the same main group, their ionic radii and polarizations are still different. It seems inappropriate to completely transpose the theories of anionic redox from Li- to Na-based systems. There are still certain issues in the earlier research of anionic redox in SIBs that are not effectively explained by current theories. The activation of damaging TM migration would be more difficult when the ionic radius of alkali and TMs differ by a large amount. Under this circumstance, sodium owns an inherent advantage and its compounds seem more stable, as shown in Na_2MnO_3 *vs.* Li_2MnO_3. Another explanation is that the interlayer distance is longer in SIBs and structural distortion can be endured during anionic redox, although Mn(3d)–O(2p) overlap is insufficient.[72] Yabuuchi and co-workers reported $Na_{2/3}[Mg_{0.28}Mn_{0.72}]O_2$ and its Li counterpart through ion exchange.[26] The latter is almost electrochemically inactive, which means that the redox activity is exclusively discovered in the Na system. It seems that the competition between cationic and anionic redox systems—to a certain extent—relies on the alkali atoms. In short, the theories of anionic redox reaction mechanism need further improvement and harmonization.

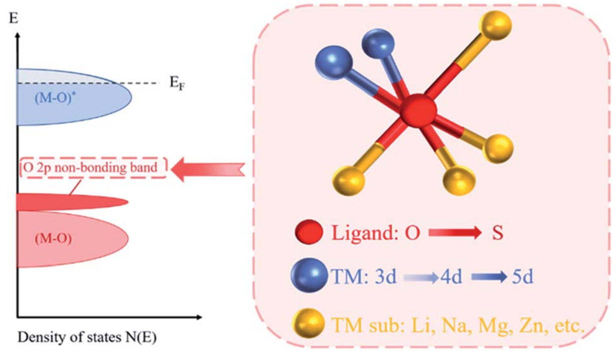

Fig. 16 Schematic illustrations of possible solutions to improve the reversibility of anionic redox in future research.

5. Characterization methods

Effective characterization is the fundamental strategy for investigating the intrinsic mechanism of anion redox. When compared with conventional TM, oxygen ions are more difficult to detect since these species are unstable and vulnerable to the environment. With technological development, a variety of useful characterization methods have been formulated that can directly or indirectly determine the electronic states of oxygen. Some promising representatives have been introduced below. It is meaningful to further advance these techniques in future studies (Fig. 17).

5.1 XPS

The principle of XPS is to utilize X-rays to radiate the samples such that the inner electrons or valence electrons of the atom are excited into emissions. The binding energy and relative intensity of the photoelectron can be measured to obtain information regarding the electronic structure of the target. XPS has been certified as a useful tool to identify the electronic states of a large range of elements, which are particularly sensitive to the electronic structural changes in metal ions.

Recently, XPS has been widely employed to investigate the oxygen redox process.[100] Rong *et al.* carried out the O1s XPS experiments to investigate the charge compensation mechanism in $Na_{0.6}[Li_{0.2}Mn_{0.8}]O_2$.[71] These spectra consist of several components derived from the oxygen crystalline network, oxygenated deposited species, and other complex organic species. The new component located at ~530.5 eV in the charged sample corresponds to the peroxo-like species, validating the contribution of the reversible oxygen redox reaction. Perez *et al.* performed XPS to simultaneously detect the electronic states of both iridium and oxygen during desodiation in Na_2IrO_3.[25] The peak of Ir, which is constant in the high-voltage range, and the emergence of a new peak of the O1s spectrum indicate that oxygen redox contributes toward the capacity of the second plateau.

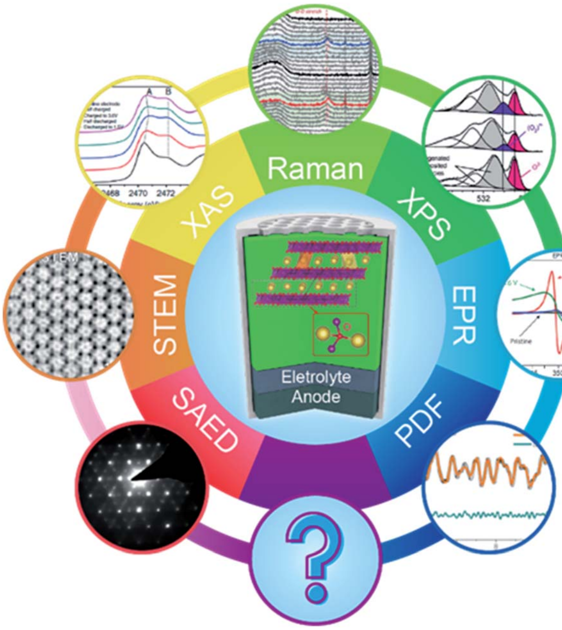

Fig. 17 Schematic illustrations of the currently accessible characterization methods for investigating the electronic and local states of oxygen.

XPS mainly provides the surface information of the specimen since the detected electrons escape from the region within about 10 nm of the material surface. The surface is easily contaminated when exposed to air during the preparation process before examination, which may influence the results. The technical conditions of XPS need to be updated, such as *in situ* measurements based on synchrotron radiation sources, in order to resolve the abovementioned issues. Moreover, bulk information should be complemented to increase characterization reliability.

5.2 XAS

XAS is definitely an effective tool to investigate the electronic structure of materials.[39] It can be further subdivided into several analytical techniques, such as XANES and EXAFS. Hard XAS (energy of electron beams is relatively higher) is a useful technique to detect heavier elements such as TMs, while soft XAS (sometimes referred to as sXAS) is particularly suitable for investigating lighter elements such as oxygen.

As for TM ions, Rong *et al.* obtained the normalized Mn K-edge XANES spectra of $Na_{0.72}[Li_{0.24}Mn_{0.76}]O_2$ electrodes at different charged and discharged states.[72] The Mn K-edge spectrum exhibits only a marginal change in the shape without any edge shifts, which implied that the valence of Mn^{4+} was constant with a change in the Mn local environment. Boisse *et al.* investigated Ru L_3-edge XAS, which investigated the Ru 4d orbitals to clarify the role of Ru during charge compensation.[24] *In situ* XAS was conducted by Susanto *et al.* to detect the Fe K-edge, and it is a powerful technique to monitor real-time changes in the electronic states during cycling.[81]

Anionic redox can be detected by sXAS, which can be operated under different modes, including the total electron yield (TEY) and partial fluorescence yield (PFY). The former is sensitive toward the surface (~5 nm), while the latter can investigate the bulk environment (~100 nm). Rong and co-workers measured the oxygen K-edge of sXAS to probe the unhybridized state of oxygen.[72] The pre-edge peak is associated with the hybridization between the O 2p orbitals and Mn 3d orbitals, while the broad peak reflects the mixing of O 2p and Mn 4sp bands. A significant change in the pre-edge peak can be ascribed to electron loss and gain at the O 2p band. Maitra *et al.* employed sXAS to investigate the origin of the extra capacity beyond TM oxidation.[44] The area under the spectra corresponds to the density of empty states above the Fermi level. *In situ* oxygen K-edge XAS can be developed like that for TMs in future research.

Resonant inelastic X-ray scattering (RIXS) is an advanced spectroscopic technique that can yield information regarding the intrinsic excitation of materials by detecting the energy and momentum differences in the scattered photons. When compared with XAS that contains the primary photon process, RIXS includes the processes of absorption and secondary photon emission, which can provide rich information; however, it suffers from lower signal intensity. It is used to study the electronic structural information such as electronic transition and charge transfer of the conduction band, valence band, and low-energy excited state. Maitra *et al.* conducted RIXS to determine the electronic structure of oxygen.[44] The evident change in the spectral weight around the plateau region implies the generation of holes on the O 2p band.

5.3 Raman

Raman spectroscopy can be used to analyze the scattering spectrum whose frequency is different from that of the incident light to obtain information on molecular vibrations and rotations. Therefore, it is sensitive to molecular bonding and the structure of the sample. It is a good alternative to XAS and has been verified to be an effective means to investigate peroxide-/superoxide-like species. At present, both *in situ* and *ex situ* tests have been widely applied in various research initiatives. Zhang *et al.* performed *in situ* Raman spectroscopy to trace the oxygen redox evolution.[94] Upon the process of oxygen redox reaction, O–O stretching was influenced and was consequently reflected in the spectrum with a shift in the peaks related to the peroxo-like O–O stretching. The formation of new peaks around ~1109 cm^{-1} corresponds to the emergence of superoxide species that are responsible for the irreversible oxygen loss and subsequent capacity fading.

5.4 TEM

TEM is a means for visualizing and characterizing the morphology and structure of the samples at the atomic scale. It can be divided into different modes, among which scanning transmission electron microscopy (STEM) and selected area electron diffraction (SAED) are the most widely used.

Both high-angle annular dark-field (HAADF) and annular bright field (ABF) STEM collect the elastically scattered electrons to yield the surface structure of the samples. HAADF-

STEM is relatively sensitive to heavier elements, including TM, while the ABF-STEM technique can accurately reveal the positions of lighter elements (such as Li and O) in the presence of atomic entities. Perez and co-workers performed ABF-STEM to visualize the atomic columns of O and residual Na atoms in charged $Na_{0.5}IrO_3$.[25] The ABF intensity profiles exhibit two sets of projected O–O separations with different distances. Li *et al.* performed a combination measurement of both HAADF and ABF modes to investigate the structural evolution upon the desodiation of $Na_2Mn_3O_7$, clearly revealing a native vacancy in the M–O slabs and Na layer between the TM slabs.[47] No Mn migration or surface reconstruction was observed, which explains the structural stability.

Electron energy loss spectroscopy (EELS) is used to measure the energy loss of the inelastically scattered electrons for composition determination and electronic state analysis. Susanto *et al.* obtained the EELS spectra from surface to bulk to determine the homogeneity of the chemical environment in charged Na_xFeO_2 since EELS can detect local areas even at the sub-nanoscale.[81] It is worth mentioning that although EELS is an effective alternative to XAS to investigate the unoccupied DOS, EELS has relatively poor resolution than that of NEXAFS, which may lead to certain loss of detailed information. In addition, EELS requires a very thin specimen and the problem of sample damage cannot be ignored since the converged electron beam energy is relatively high.

SAED is a powerful tool to obtain information regarding spatial configuration. The SAED patterns of the two polymorphs of Na_2RuO_3 show distinct characteristics such as those reported by Boisse *et al.*[24] The extra diffraction spots in the SAED pattern of ordered Na_2RuO_3 can be indexed to a super cell arising from the honeycomb ordering in the TM slabs. This feature was also observed in charged Na_1RuO_3, proving the existence of the ordered intermediate phase. Susanto analyzed the SAED pattern of $Na_{1-x}FeO_2$ and observed the formation of spinel Fe_3O_4, which partially explains the rapid capacity decay in α-$NaFeO_2$.[81]

5.5 Other characterizations

PDF that can be used to collect the total scattering data can provide real-space information. Local distortion and structural ordering in a short range can be determined. It can be utilized to characterize the local oxidized species generated during the redox process. It can be divided into X-ray PDF (xPDF) and neutron PDF (nPDF) according to the scattering light source. The former is relatively sensitive to heavy atoms and therefore can effectively probe the TM framework, while the latter can be utilized to detect oxygen environments both locally and averagely. The total scattering data from the reciprocal space can also be applied for performing structural refinements in materials to perform quantitative structural analysis.

Electronic paramagnetic resonance (EPR) is a helpful spectroscopy technique that detects single-spin or radical species. It is also an alternative tool to probe peroxo-like species appearing during the anionic redox reaction, which can be developed in future research and applied for studying anionic redox reactions in SIBs.

Operando UV-vis measurements are a helpful tool to analyze and determine the composition and structure of a substance by the degree of absorption in ranges of UV and visible light. It was utilized by Otoyama *et al.* to investigate the underlying mechanism of capacity decay in Na_3RuO_4.[93]

Cyclic voltammetry (CV) and/or the dQ/dV curve is a commonly used electrochemical analysis method, reflecting the essential behavior of an electrochemical process that could provide preliminary information on the reversibility of the electrode reaction and the possibility of the formation of a new phase. For research on anionic redox, the peaks appearing in the curves help us to pinpoint the various nodes of reaction processes and perform the above characterization methods to further investigate the oxygen activity.

6. Conclusion and prospects

The practical development of environmentally friendly and renewable energy is on the basis of ideal large-scale energy storage systems. SIB as a good alternative to lithium-ion batteries has been extensively studied in the recent years. The relatively small specific capacity of SIBs has always been a roadblock, which hinders its practical applications. Anionic redox provides a new perspective for designing high-capacity cathode materials for SIBs. A series of related articles have been published with outstanding performance and novel discoveries. The inherent mechanism of anionic redox is under a controversial debate. Here, we give a systematic review of the recent related research on anionic redox reactions in SIBs with the hope of facilitating future research.

In this review, we give an overview of the fundamental theories, reported anionic redox materials, current challenges, and possible solutions together with effective characterization techniques to provide a deeper insight into the anionic redox reaction. According to current theories, the specific structure that can generate oxygen lone pairs (or O 2p nonbonding band in the band structure) is the significant premise to achieve anionic redox. Highly covalent M–O bonding is another requisite for realizing reversible anionic redox. It is worthy to mention that there is still a fierce controversy regarding this issue. The metastable peroxo-like species (O holes in the band structure) can be stabilized through $M-(O_2)^{n-}$ interactions along with oxygen network reorganization (splitting of the degenerated ground state), which is termed as the reductive coupling mechanism. Another possibility is the generation of localized electron holes on the O atoms to achieve the localization of the peroxide species.

Through the overview of the reported materials that utilize the anionic redox reaction, it can be determined that various structural configurations can induce the emergence of O 2p nonbonding bands, including Li–O–Li, Na–O–Na, Na–O–Mg/Zn/□, □–O–□, *etc.* The present major difficulty in anionic redox is irreversibility. Among them, the Na–O–Mg/□ configuration is relatively superior since $Na_{2/3}[Mg_{0.28}Mn_{0.72}]O_2$ and $Na_{4/7}[\square_{1/7}Mn_{6/7}]O_2$ have been reported to yield relatively better cycling stability. Related modifications can be studied in future research. From this perspective, other innovative configurations that can induce oxygen redox should be explored to broaden the range of anionic redox materials. Most of the materials currently under investigation are manganese-based layered oxides. It has been proposed that manganese has deficient covalency with oxygen to realize the reductive coupling mechanism. Therefore, materials with characteristics of high covalency between metals and ligands can be explored. For example, introducing other TMs with proper electronegativity (generally on the right-hand side of the periodic table), as well as other anions such as sulfur. When compared with electrodes with 4d or 5d TMs, the abovementioned materials have higher economic efficiency. Advanced theoretical calculations can be applied as a powerful tool to help predict and design potential materials for reversible anionic redox.

It should be noted that future studies do not have to be completely based on existing theories. On one hand, it is not feasible to completely transpose the mechanism of anionic redox from Li- to Na-based systems. Moreover, it has already been reported that the lithium counterpart of specific Na-based materials do not exhibit electrochemical activity. On the other hand, current theories can be further improved in a comprehensive manner based on the development of more advanced characterization techniques.

In conclusion, we have demonstrated a systematic summary of the recent research regarding anionic redox reactions in SIBs, aimed at giving a comprehensive understanding of the anionic redox reaction. It is promising to apply anionic redox to facilitate the development of high-capacity electrode materials for SIBs.

Conflicts of interest

There are no conflicts to declare.

Acknowledgements

This work was partially supported financially by National Basic Research Program of China (2018YFB0104302), NSF of China (21633003, 51802149 and U1801251) and NSF of Jiangsu Province, China (BK20170630) and the Fundamental Research Funds for the Central Universities (021314380141 and 021314380157).

References

1 B. Dunn, H. Kamath and J. M. Tarascon, *Science*, 2011, **334**, 928.
2 J. M. Tarascon, *Nat. Chem.*, 2010, **2**, 510.
3 M. S. Whittingham, *Chem. Rev.*, 2014, **114**, 11414–11443.
4 M. D. Slater, D. Kim, E. Lee and C. S. Johnson, *Adv. Funct. Mater.*, 2013, **23**, 947–958.
5 S. Komaba, W. Murata, T. Ishikawa, N. Yabuuchi, T. Ozeki, T. Nakayama, A. Ogata, K. Gotoh and K. Fujiwara, *Adv. Funct. Mater.*, 2011, **21**, 3859–3867.
6 S.-W. Kim, D.-H. Seo, X. Ma, G. Ceder and K. Kang, *Adv. Energy Mater.*, 2012, **2**, 710–721.
7 J. Y. Hwang, S. T. Myung and Y. K. Sun, *Chem. Soc. Rev.*, 2017, **46**, 3529–3614.
8 C. Fang, Y. Huang, W. Zhang, J. Han, Z. Deng, Y. Cao and H. Yang, *Adv. Energy Mater.*, 2016, **6**, 1501727.
9 S. Kumakura, Y. Tahara, S. Sato, K. Kubota and S. Komaba, *Chem. Mater.*, 2017, **29**, 8958–8962.
10 N. Yabuuchi, M. Kajiyama, J. Iwatate, H. Nishikawa, S. Hitomi, R. Okuyama, R. Usui, Y. Yamada and S. Komaba, *Nat. Mater.*, 2012, **11**, 512–517.
11 S. Guo, Q. Li, P. Liu, M. Chen and H. Zhou, *Nat. Commun.*, 2017, **8**, 135.
12 S. Guo, P. Liu, H. Yu, Y. Zhu, M. Chen, M. Ishida and H. Zhou, *Angew. Chem. Int. Ed.*, 2015, **54**, 5894–5899.
13 A. Grimaud, W. T. Hong, Y. Shao-Horn and J. M. Tarascon, *Nat. Mater.*, 2016, **15**, 121–126.
14 N. Yabuuchi, *Chem. Lett.*, 2017, **46**, 412–422.
15 M. Sathiya, G. Rousse, K. Ramesha, C. P. Laisa, H. Vezin, M. T. Sougrati, M. L. Doublet, D. Foix, D. Gonbeau, W. Walker, A. S. Prakash, M. Ben Hassine, L. Dupont and J. M. Tarascon, *Nat. Mater.*, 2013, **12**, 827–835.
16 H. Koga, L. Croguennec, M. Ménétrier, K. Douhil, S. Belin, L. Bourgeois, E. Suard, F. Weill and C. Delmas, *J. Electrochem. Soc.*, 2013, **160**, A786–A792.
17 Z. Lu and J. R. Dahn, *J. Electrochem. Soc.*, 2002, **149**, A815–A822.
18 M. Sathiya, K. Ramesha, G. Rousse, D. Foix, D. Gonbeau, A. S. Prakash, M. L. Doublet, K. Hemalatha and J. M. Tarascon, *Chem. Mater.*, 2013, **25**, 1121–1131.
19 E. McCalla, A. M. Abakumov, M. Saubanere, D. Foix, E. J. Berg, G. Rousse, M. L. Doublet, D. Gonbeau, P. Novak, G. V. Tandeloo, R. Dominko and J. M. Tarascon, *Science*, 2015, **350**, 1218.
20 C. Zhao, Q. Wang, Y. Lu, Y.-S. Hu, B. Li and L. Chen, *J. Phys. D: Appl. Phys.*, 2017, **50**, 183001.
21 K. Du, J. Zhu, G. Hu, H. Gao, Y. Li and J. B. Goodenough, *Energy Environ. Sci.*, 2016, **9**, 2575–2577.
22 M. Kalapsazova, G. F. Ortiz, J. L. Tirado, O. Dolotko, E. Zhecheva, D. Nihtianova, L. Mihaylov and R. Stoyanova, *ChemPlusChem*, 2015, **80**, 1642–1656.
23 J. Xu, D. H. Lee, R. J. Clément, X. Yu, M. Leskes, A. J. Pell, G. Pintacuda, X.-Q. Yang, C. P. Grey and Y. S. Meng, *Chem. Mater.*, 2014, **26**, 1260–1269.
24 B. Mortemard de Boisse, G. Liu, J. Ma, S. I. Nishimura, S. C. Chung, H. Kiuchi, Y. Harada, J. Kikkawa, Y. Kobayashi, M. Okubo and A. Yamada, *Nat. Commun.*, 2016, **7**, 11397.
25 A. J. Perez, D. Batuk, M. Saubanère, G. Rousse, D. Foix, E. McCalla, E. J. Berg, R. Dugas, K. H. W. van den Bos, M.-L. Doublet, D. Gonbeau, A. M. Abakumov, G. Van Tendeloo and J.-M. Tarascon, *Chem. Mater.*, 2016, **28**, 8278–8288.
26 N. Yabuuchi, R. Hara, K. Kubota, J. Paulsen, S. Kumakura and S. Komaba, *J. Mater. Chem. A*, 2014, **2**, 16851–16855.
27 N. Yabuuchi, R. Hara, M. Kajiyama, K. Kubota, T. Ishigaki, A. Hoshikawa and S. Komaba, *Adv. Energy Mater.*, 2014, **4**, 1301453.
28 J. Rouxel, *Chem.–Eur. J.*, 1996, **2**(9), 1053–1059.

29 J. M. Tarascon, G. Vaughan, Y. Chabre, L. Seguin, M. Anne, P. Strobel and G. Amatucci, *J. Solid State Chem.*, 1999, **147**, 410–420.

30 M. K. Aydinol, A. F. Kohan and G. Ceder, *Phys. Rev. B: Condens. Matter Mater. Phys.*, 1997, **56**(3), 1354–1365.

31 G. Ceder, Y.-M. Chiang, D. R. Sadoway, M. K. Aydinol, Y.-I. Jang and B. Huang, *Nature*, 1998, **329**, 416.

32 P. Kalyani, S. Chitra, T. Mohan and S. Gopukumar, *J. Power Sources*, 1999, **80**, 103–106.

33 A. D. Robertson and P. G. Bruce, *Chem. Mater.*, 2003, **15**, 1984–1992.

34 K. Luo, M. R. Roberts, R. Hao, N. Guerrini, D. M. Pickup, Y. S. Liu, K. Edstrom, J. Guo, A. V. Chadwick, L. C. Duda and P. G. Bruce, *Nat. Chem.*, 2016, **8**, 684–691.

35 A. R. Armstrong, M. Holzapfel, P. Novak, C. S. Johnson, S. Kang, M. M. Thackeray and P. G. Bruce, *J. Am. Chem. Soc.*, 2006, **128**, 8694–8698.

36 A. Boulineau, L. Simonin, J. Colin, C. Bourbon and S. Patoux, *Nano Lett.*, 2013, **13**, 3857–3863.

37 S. Muhammad, H. Kim, Y. Kim, D. Kim, J. H. Song, J. Yoon, J.-H. Park, S.-J. Ahn, S.-H. Kang, M. M. Thackeray and W.-S. Yoon, *Nano Energy*, 2016, **21**, 172–184.

38 H. Koga, L. Croguennec, M. Ménétrier, P. Mannessiez, F. Weill and C. Delmas, *J. Power Sources*, 2013, **236**, 250–258.

39 H. Koga, L. Croguennec, M. Ménétrier, P. Mannessiez, F. Weill, C. Delmas and S. Belin, *J. Phys. Chem. C*, 2014, **118**, 5700–5709.

40 G. Assat, A. Iadecola, C. Delacourt, R. Dedryvère and J.-M. Tarascon, *Chem. Mater.*, 2017, **29**, 9714–9724.

41 P. E. Pearce, A. J. Perez, G. Rousse, M. Saubanere, D. Batuk, D. Foix, E. McCalla, A. M. Abakumov, G. Van Tendeloo, M. L. Doublet and J. M. Tarascon, *Nat. Mater.*, 2017, **16**, 580–586.

42 M. Sathiya, A. M. Abakumov, D. Foix, G. Rousse, K. Ramesha, M. Saubanere, M. L. Doublet, H. Vezin, C. P. Laisa, A. S. Prakash, D. Gonbeau, G. VanTendeloo and J. M. Tarascon, *Nat. Mater.*, 2015, **14**, 230–238.

43 N. Yabuuchi, K. Yoshii, S. T. Myung, I. Nakai and S. Komaba, *J. Am. Chem. Soc.*, 2011, **133**, 4404–4419.

44 U. Maitra, R. A. House, J. W. Somerville, N. Tapia-Ruiz, J. G. Lozano, N. Guerrini, R. Hao, K. Luo, L. Jin, M. A. Perez-Osorio, F. Massel, D. M. Pickup, S. Ramos, X. Lu, D. E. McNally, A. V. Chadwick, F. Giustino, T. Schmitt, L. C. Duda, M. R. Roberts and P. G. Bruce, *Nat. Chem.*, 2018, **10**, 288–295.

45 X. Bai, M. Sathiya, B. Mendoza-Sánchez, A. Iadecola, J. Vergnet, R. Dedryvère, M. Saubanère, A. M. Abakumov, P. Rozier and J.-M. Tarascon, *Adv. Energy Mater.*, 2018, **8**, 1802379.

46 B. Mortemard de Boisse, S.-i. Nishimura, E. Watanabe, L. Lander, A. Tsuchimoto, J. Kikkawa, E. Kobayashi, D. Asakura, M. Okubo and A. Yamada, *Adv. Energy Mater.*, 2018, **8**, 1800409.

47 Y. Li, X. Wang, Y. Gao, Q. Zhang, G. Tan, Q. Kong, S. Bak, G. Lu, X.-Q. Yang, L. Gu, J. Lu, K. Amine, Z. Wang and L. Chen, *Adv. Energy Mater.*, 2019, **9**, 1803087.

48 G. Assat and J.-M. Tarascon, *Nat. Energy*, 2018, **3**, 373–386.

49 Y. You and A. Manthiram, *Adv. Energy Mater.*, 2018, **8**, 1701785.

50 J. B. Goodenough and Y. Kim, *Chem. Mater.*, 2010, **22**, 587–603.

51 Y. Xie, M. Saubanère and M. L. Doublet, *Energy Environ. Sci.*, 2017, **10**, 266–274.

52 M. Ben Yahia, J. Vergnet, M. Saubanere and M. L. Doublet, *Nat. Mater.*, 2019, **18**, 496–502.

53 M. Saubanère, E. McCalla, J. M. Tarascon and M. L. Doublet, *Energy Environ. Sci.*, 2016, **9**, 984–991.

54 D. H. Seo, J. Lee, A. Urban, R. Malik, S. Kang and G. Ceder, *Nat. Chem.*, 2016, **8**, 692–697.

55 B. Li and D. Xia, *Adv. Mater.*, 2017, **29**, 1701054.

56 J. Zaanen, G. A. Sawatzky and J. W. Allen, *Phys. Rev. Lett.*, 1985, **55**, 418–421.

57 A. R. Armstrong, M. Holzapfel, P. Novak, C. S. Johnson, S. H. Kang, M. M. Thackeray and P. G. Bruce, *J. Am. Chem. Soc.*, 2006, **128**, 8694–8698.

58 D. Y. W. Yu, K. Yanagida, Y. Kato and H. Nakamura, *J. Electrochem. Soc.*, 2009, **156**, A417–A424.

59 C. S. Johnson, J. S. Kim, C. Lefief, N. Li, J. T. Vaughey and M. M. Thackeray, *Electrochem. Commun.*, 2004, **6**, 1085–1091.

60 B. Strehle, K. Kleiner, R. Jung, F. Chesneau, M. Mendez, H. A. Gasteiger and M. Piana, *J. Electrochem. Soc.*, 2017, **164**, A400–A406.

61 B. Li, R. Shao, H. Yan, L. An, B. Zhang, H. Wei, J. Ma, D. Xia and X. Han, *Adv. Funct. Mater.*, 2016, **26**, 1330–1337.

62 S. Kim, M. Aykol, V. I. Hegde, Z. Lu, S. Kirklin, J. R. Croy, M. M. Thackeray and C. Wolverton, *Energy Environ. Sci.*, 2017, **10**, 2201–2211.

63 E. Talaie, S. Y. Kim, N. Chen and L. F. Nazar, *Chem. Mater.*, 2017, **29**, 6684–6697.

64 S. Komaba, N. Yabuuchi, T. Nakayama, A. Ogata, T. Ishikawa and I. Nakai, *Inorg. Chem.*, 2012, **51**, 6211–6220.

65 W. Kong, R. Gao, Q. Li, W. Yang, J. Yang, L. Sun and X. Liu, *J. Mater. Chem. A*, 2019, **7**, 9099–9109.

66 C. Ma, J. Alvarado, J. Xu, R. J. Clement, M. Kodur, W. Tong, C. P. Grey and Y. S. Meng, *J. Am. Chem. Soc.*, 2017, **139**, 4835–4845.

67 Z. Lu and J. R. Dahn, *J. Electrochem. Soc.*, 2001, **14**, A1225–A1229.

68 T. Risthaus, D. Zhou, X. Cao, X. He, B. Qiu, J. Wang, L. Zhang, Z. Liu, E. Paillard, G. Schumacher, M. Winter and J. Li, *J. Power Sources*, 2018, **395**, 16–24.

69 H. Yu, G. Liu, G. Li, J. Zhang, G. Chen and L. Wen, *Electrochim. Acta*, 2018, **263**, 474–479.

70 E. de la Llave, E. Talaie, E. Levi, P. K. Nayak, M. Dixit, P. T. Rao, P. Hartmann, F. Chesneau, D. T. Major, M. Greenstein, D. Aurbach and L. F. Nazar, *Chem. Mater.*, 2016, **28**, 9064–9076.

71 X. Rong, J. Liu, E. Hu, Y. Liu, Y. Wang, J. Wu, X. Yu, K. Page, Y.-S. Hu, W. Yang, H. Li, X.-Q. Yang, L. Chen and X. Huang, *Joule*, 2018, **2**, 125–140.

72 X. Rong, E. Hu, Y. Lu, F. Meng, C. Zhao, X. Wang, Q. Zhang, X. Yu, L. Gu, Y.-S. Hu, H. Li, X. Huang, X.-Q. Yang, C. Delmas and L. Chen, *Joule*, 2019, **3**, 503–517.

73 D. Kim, M. Cho and K. Cho, *Adv. Mater.*, 2017, **29**, 1701788.
74 X. Rong, F. Gao, Y. Lu, K. Yang and Y. Hu, *Chin. Chem. Lett.*, 2018, **29**, 1791–1794.
75 E. McCalla, A. W. Rowe, J. Camardese and J. R. Dahn, *Chem. Mater.*, 2013, **25**, 2716–2721.
76 E. Adamczyk and V. Pralong, *Chem. Mater.*, 2017, **29**, 4645–4648.
77 Q. Wang, W. Yang, F. Kang and B. Li, *Energy Storage Materials*, 2018, **14**, 361–366.
78 F. M. Chang and M. Jansen, *Z. Anorg. Allg. Chem.*, 1985, **631**, 177–182.
79 E. A. Raekelboom, A. L. Hector, J. Owen, G. Vitins and M. T. Weller, *Chem. Mater.*, 2001, **13**, 4618–4623.
80 N. Yabuuchi, H. Yoshida and S. Komaba, *Electrochemistry*, 2012, **80**, 716–719.
81 D. Susanto, M. K. Cho, G. Ali, J.-Y. Kim, H. J. Chang, H.-S. Kim, K.-W. Nam and K. Y. Chung, *Chem. Mater.*, 2019, **31**, 3644–3651.
82 Y. Li, Y. Gao, X. Wang, X. Shen, Q. Kong, R. Yu, G. Lu, Z. Wang and L. Chen, *Nano Energy*, 2018, **47**, 519–526.
83 Y. Gao, Z. Wang and G. Lu, *J. Mater. Chem. A*, 2019, **7**, 2619–2625.
84 H. Yoshida, N. Yabuuchi and S. Komaba, *Electrochem. Commun.*, 2013, **34**, 60–63.
85 N. Yabuuchi, M. Yano, H. Yoshida, S. Kuze and S. Komaba, *J. Electrochem. Soc.*, 2013, **160**, A3131–A3137.
86 B. Su, J. Zhang, M. Fujita, W. Zhou, P. H. L. Sit and D. Y. W. Yu, *J. Electrochem. Soc.*, 2018, **166**, A5075–A5080.
87 Z. Shadike, Y. N. Zhou, L. L. Chen, Q. Wu, J. L. Yue, N. Zhang, X. Q. Yang, L. Gu, X. S. Liu, S. Q. Shi and Z. W. Fu, *Nat. Commun.*, 2017, **8**, 566.
88 M. Tamaru, X. Wang, M. Okubo and A. Yamada, *Electrochem. Commun.*, 2013, **33**, 23–26.
89 H. Kobayashi, R. Kanno, Y. Kawamoto, M. Tabuchi, O. Nakamura and M. Takano, *Solid State Ionics*, 1995, **82**, 25–31.
90 K. M. Mogare, K. Friese, W. Klein and M. Jansen, *Z. Anorg. Allg. Chem.*, 2004, **630**, 547–552.
91 P. Rozier, M. Sathiya, A.-R. Paulraj, D. Foix, T. Desaunay, P.-L. Taberna, P. Simon and J.-M. Tarascon, *Electrochem. Commun.*, 2015, **53**, 29–32.
92 Y. Qiao, S. Guo, K. Zhu, P. Liu, X. Li, K. Jiang, C.-J. Sun, M. Chen and H. Zhou, *Energy Environ. Sci.*, 2018, **11**, 299–305.
93 M. Otoyama, Q. Jacquet, A. Iadecola, M. Saubanère, G. Rousse and J. M. Tarascon, *Adv. Energy Mater.*, 2019, **9**, 1803674.
94 X. Zhang, Y. Qiao, S. Guo, K. Jiang, S. Xu, H. Xu, P. Wang, P. He and H. Zhou, *Adv. Mater.*, 2019, e1807770, DOI: 10.1002/adma.201807770.
95 S. Venkatraman and A. Manthiram, *J. Solid State Chem.*, 2004, **177**, 4244–4250.
96 B. Ammundsen, D. J. Jones, J. Roziere and G. R. Burns, *Chem. Mater.*, 1995, **7**, 2151–2160.
97 N. Yabuuchi, M. Takeuchi, M. Nakayama, H. Shiiba, M. Ogawa, K. Nakayama, T. Ohta, D. Endo, T. Ozaki, T. Inamasu, K. Sato and S. Komaba, *Proc. Natl. Acad. Sci. U. S. A.*, 2015, **112**, 7650–7655.
98 E. Lee, S. Sahgong, C. S. Johnson and Y. Kim, *Electrochim. Acta*, 2014, **143**, 272–277.
99 D. Kim, M. Cho and K. Cho, *J. Mater. Chem. A*, 2018, **6**, 18036–18043.
100 D. Foix, M. Sathiya, E. McCalla, J.-M. Tarascon and D. Gonbeau, *J. Phys. Chem. C*, 2016, **120**, 862–874.